SCHOLAR COMMONS
USF UNIVERSITY OF SOUTH FLORIDA

University of South Florida
Scholar Commons

Graduate Theses and Dissertations

Graduate School

3-21-2003

Modeling and Characterization of Polycrystalline Mercuric Iodide Radiation Detectors

Unmesh Khadilkar
University of South Florida

Follow this and additional works at: https://scholarcommons.usf.edu/etd

Part of the American Studies Commons

Scholar Commons Citation
Khadilkar, Unmesh, "Modeling and Characterization of Polycrystalline Mercuric Iodide Radiation Detectors" (2003). *Graduate Theses and Dissertations.*
https://scholarcommons.usf.edu/etd/1405

This Thesis is brought to you for free and open access by the Graduate School at Scholar Commons. It has been accepted for inclusion in Graduate Theses and Dissertations by an authorized administrator of Scholar Commons. For more information, please contact scholarcommons@usf.edu.

MODELING AND CHARACTERIZATION OF POLYCRYSTALLINE MERCURIC IODIDE RADIATION DETECTORS

by

UNMESH KHADILKAR

A thesis submitted in partial fulfillment
of the requirements for the degree of
Master of Science in Electrical Engineering
Department of Electrical Engineering
College of Engineering
University of South Florida

Major Professor: Don Morel, Ph.D.
Dr. Christos Ferekides, Ph.D.
Dr. Y.L Chiou, Ph.D.

Date of Approval:
March 21, 2003

Keywords: HgI_2, photodetectors, optoelectronics, MEDICI, compound semiconductors

© Copyright 2003, Unmesh Khadilkar

ACKNOWLEDGEMENTS

I would like to express my gratitude to several people who have helped me throughout my research work, without whose assistance this work would not have been possible. First of all I wish to express my deep gratitude and thankfulness to Dr. Don Morel, major professor, for providing me with this opportunity to conduct this dissertation. He has personally trained and educated me and taken keen interest to aid in the development of my knowledge. He has been my mentor and has been very supportive through and through. I would like to offer my deep gratefulness to Dr Chris Ferekides for his guidance and extremely helpful insights and also for accepting to be one of my committee members. My next appreciations are due, to Dr. Y. L. Chiou, who is also a member of my advisory committee for his critical suggestions in making this a better report. I would also like to take this opportunity to immensely thank Harish Sankaranarayanan for helping me at each and every step. Genuine appreciation is directed to Lodewijk van den Berg, P. J. Simon and others who are a part of the Mercuric Iodide team at USF. Last but not the least I would like thank my co-workers at the Thin Film Compound Semiconductor Lab for making this a very fulfilling experience.

TABLE OF CONTENTS

LIST OF TABLES ii

LIST OF FIGURES iv

ABSTRACT vi

CHAPTER 1 INTRODUCTION 1
1.1 Semiconductor fundamentals 1
1.1.1 Energy bands in semiconductors 2
1.1.2 Fermi-Dirac statistics and the Fermi level 3
1.2 Carrier transport in semiconductors 5
1.2.1 Low field transport 5
1.2.2 High field transport 5
1.3 Optical absorption in semiconductors 6
1.4 Photoconductors 7
1.5 Compound semiconductors 9
1.6 Mercuric iodide 10
1.6.1 Crystal structure 10
1.7 Objective of research 12
1.8 Literature review 13

CHAPTER 2 MEASUREMENTS ON POLYCRYSTALLINE FILMS 15
2.1 Film structure and layout 16
2.2 Optical measurements 17

CHAPTER 3 POLYCRYSTALLINE FILM SIMULATION 21
3.1 Film #05-08-02 21
3.2 Film #09-17-02 27
3.3 Film #10-02-02 32
3.4 Film #10-03-02 37
3.5 Qualitative analysis and conclusions 42

CHAPTER 4 CONCLUSIONS 44
4.1 Conclusion 44
4.2 Future work 45

REFERENCES 47

APPENDICES 49
Appendix 1 MEDICI^{tm} 50

LIST OF TABLES

Table 1.1 Crystallographic data of α-HgI_2 11

Table 2.1 Deposition parameters 17

Table 2.2 List of peak quantum efficiencies @ -50V 18

Table 2.3 List of peak dark currents @ -50V 19

Table 3.1 Deposition parameters of film #05-08-02 21

Table 3.2 Transport parameters for film #05-08-02 25

Table 3.3 Absorption data for film #05-08-02 25

Table 3.4 Deposition parameters of film #09-17-02 27

Table 3.5 Transport parameters for film #09-17-02 30

Table 3.6 Absorption data for film #09-17-02 30

Table 3.7 Peak quantum efficiencies and dark currents for film #09-17-02 31

Table 3.8 Deposition parameters for film #10-02-02 32

Table 3.9 Transport parameters for film #10-02-02 35

Table 3.10 Absorption data for film #10-02-02 36

Table 3.11 Peak quantum efficiencies and dark currents for film #10-02-02 37

Table 3.12 Deposition parameters for film #10-03-02 37

Table 3.13 Transport parameters for film #10-03-02 41

Table 3.14 Absorption data for film #10-03-02 41

Table 3.15 Peak quantum efficiencies and dark currents for film #10-02-02 42

Table 3.16 Comparison of generated and measured parameters 43

LIST OF FIGURES

Figure 1.1 Band structures of direct and indirect band semiconductors 3

Figure 1.2 (a) Geometry of a photoconductor (b) Typical bias circuit for a photodetector 8

Figure 1.3 Schematic of bias circuit used for measurements 9

Figure 1.4 Elemental cell of tertragonal α-HgI_2 12

Figure 2.1 Layout of a typical polycrystalline film 16

Figure 3.1 #05-08-02 Spectral response @ -50V 22

Figure 3.2 #05-08-02 Light I-V characteristics @ 582.5nm 22

Figure 3.3 #05-08-02 Light I-V characteristics @ 600nm 23

Figure 3.4 #05-08-02 Light I-V characteristics @ 620nm 23

Figure 3.5 #05-08-02 Absorption data 24

Figure 3.6 #09-17-02 Spectral response @ -50V 27

Figure 3.7 #09-17-02 Light I-V characteristics @ 582.5nm 28

Figure 3.8 #09-17-02 Light I-V characteristics @ 600nm 28

Figure 3.9 #09-17-02 Light I-V characteristics @ 620nm 29

Figure 3.10 #09-17-02 Absorption data 29

Figure 3.11 #10-02-02 Spectral response @ -50V 33

Figure 3.12 #10-02-02 Light I-V characteristics @ 582.5nm 33

Figure 3.13 #10-02-02 Light I-V characteristics @ 600nm 34

Figure 3.14 #10-02-02 Light I-V characteristics @ 620nm 34

Figure 3.15 #10-02-02 Absorption data 35

Figure 3.16 #10-03-02 Spectral response @ -50V 38

Figure 3.17 #10-03-02 Light I-V characteristics @ 582.5nm 39

Figure 3.18 #10-03-02 Light I-V characteristics @ 600nm 39

Figure 3.19 #10-03-02 Light I-V characteristics @ 620nm 40

Figure 3.20 #10-03-02 Absorption data 40

Figure 3.21 Comparison of absorption properties generated from simulations 44

MODELING AND CHARACTERIZATION OF POLYCRYSTALLINE

MERCURIC IODIDE RADIATION DETECTORS

Unmesh Khadilkar

ABSTRACT

The ability of Mercuric Iodide (HgI_2) to function as a highly efficient radiation detector at room temperature has generated great interest and has triggered further studies on this difficult material. This property is expected to enable significant enhancements to a far-ranging variety of applications and systems. HgI_2 devices have shown superior performance at room temperature compared to elemental Si or Ge devices, which require to be cooled down to liquid nitrogen temperature when used as nuclear radiation detectors. While substantial studies have been conducted on single crystal HgI_2, polycrystalline HgI_2 remains a comparatively less studied form of this material.

The primary use of HgI_2 is as a direct radiation detector. It can also be used in applications with a scintillator intermediate to generate visible light from incident nuclear radiation. Hence its response to visible light can be used to study the electronic properties of HgI_2 polycrystalline films.

The films are deposited on TEC-15 LOF glass with a Tin Oxide($Sn0_2$) coating which acts as the growth surface. It also acts as the front contact with Palladium(Pd) being the back contact. Wire leads are attached to the palladium for electrical contact. The deposited films are circular in shape with a diameter of 2.5cm with thickness ranging

from 50 to 600µm. A maximum of 7 devices are contacted at various points on every film.

For the measurements documented in this thesis, a tungsten-halogen lamp and an Oriel 1/4m grating monochromator are used as a light source. The incident flux on the sample is determined using a Si photodiode as reference. Device performance for both single crystal as well as polycrystalline films is documented. We have attempted to identify a set of optimum growth parameters using these measurements. For a film to be considered favorably, not only should the individual devices show high quantum efficiencies and low dark currents, but the response of all devices on the same film should be uniform. A number of films are studied and the optimum film deposition conditions are commented upon.

A powerful semiconductor device simulation tool, MEDICI^{tm}, is used to simulate the photoresponse of these films. The simulations are compared to the measurements and the transport and light absorption parameters of the polycrystalline films are determined.

CHAPTER 1

INTRODUCTION

1.1 Semiconductor fundamentals

Materials can be categorized into conductors, insulators and semiconductors. This categorization is made on the basis of the electrical properties of these materials. The difference between these categories can be explained by the band theory of materials. All materials are composed of individual elements, which in unit form consist of an atomic nucleus surrounded by electrons in different orbits. Electrons occupy energy levels from the lower energy upwards. These energy levels form bands. The highest filled band is known as the valence band. The next allowed energy level above the valence band is the conduction band. The energy difference between the valence and conduction bands is known as the band-gap. This band-gap is nearly negligible in metals. Often in metals, the conduction and valence bands overlap allowing free transition of electrons between the bands. Insulators are materials where the band-gap is large enough that no electrons can transit from the valence band to the conduction band. Semiconductors are essentially insulators, which begin conducting under special circumstances. They have a measurably large band-gap i.e. the valence and conduction bands are separated by a forbidden energy gap.

1.1.1 Energy bands in semiconductors

The highest band, which holds electrons in the ground state, is known as the valence band, while the lowest empty band is known as the conduction band. The energy gap that separates these bands is known as the band-gap. For semiconductors this gap is between 0 to 3eV. Consider a valence band in ground state. The total crystal Momentum for this band is zero because for every occupied k-state there exists a corresponding filled state with opposite momentum. The top of the valence band for most semiconductors occurs at k=0 i.e. at effective momentum equal to zero. The bottom of the conduction band in direct semiconductors occurs at k=0. Such semiconductors show interaction with light due to the alignment of the conduction and valence band edges. Band transitions for such semiconductors can be initiated by incident radiation. For indirect semiconductors the bottom of the conduction band does not occur at k=0. Fig. 1.1 [1] explains the difference between direct and indirect semiconductors.

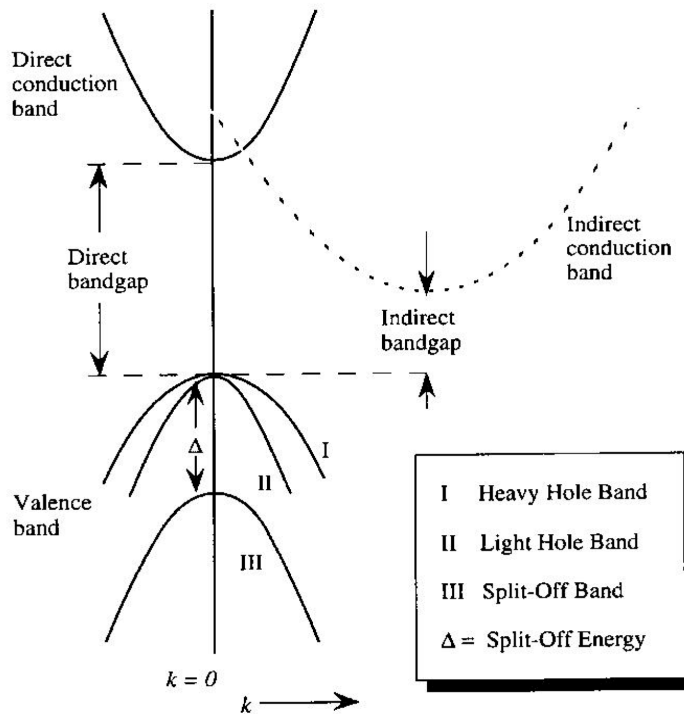

Figure 1.1 Band structures of direct and indirect band semiconductors

1.1.2 Fermi-Dirac statistics and the Fermi level

Fermi-Dirac theory governs the behavior of a class of particles called fermions. According to this theory, no two fermions can occupy the same Eigen state. Electrons, protons and neutrons are all fermions. This theory is the basis of explaining why electrons are arranged in orbitals around the nucleus of an atom and do not collapse into a common state.

Consider the case of the intrinsic semiconductor. The number of occupied conduction band levels is [2]

$$n = \int_{Ec}^{Etop} N(E)F(E)dE \qquad 1.1$$

where,

F(E) : Fermi-Dirac distribution function.

N(E)dE : density of energy states with energies between *Ec* and *Etop.*

Ec, Etop : Lower and upper levels of energy band under consideration.

The Fermi-Dirac distribution is given by

$$F(E)=\frac{1}{1+\exp(\frac{E-Ef}{kT})} \qquad 1.2$$

Eq.1.2 can be modified further to give

$$n= Nc\exp(\frac{-(Ec-Ef)}{kT}) \qquad 1.3$$

where,

Nc : electron density in conduction band.

Ef : Fermi level.

Similarly hole density near valence band top is given by

$$p= Nv\exp(\frac{-(Ef-Ev)}{kT}) \qquad 1.4$$

where,

Nv : hole density in valence band.

In intrinsic semiconductors, continuous thermal agitation exists at finite temperatures. This results in excitation of electrons to the conduction band and leaves behind an equal number of holes in the valence band. The probability of an electron having sufficient energy to make this transition is given by the Fermi distribution function. The Fermi Level is the energy level at which the probability function is equal to one half. Thus the Fermi Level of an intrinsic semiconductor is thus very close to the middle of the forbidden gap. Though none of the electrons actually have energy of E_f

because they're not permitted to exist at energies in the band-gap. The energy band diagram is referenced to a value known as the vacuum potential. The electron affinity, $q\chi$ is the energy required to remove an electron from the conduction band to the vacuum potential.

1.2 Carrier transport in semiconductors

Consider a beam of electrons moving initially with the same momentum. Due to the scattering process the momentum and energy will gradually lose coherence with the initial state values. The average time it takes to lose coherence or memory with initial state values is called the relaxation time or scattering time [2].

1.2.1 Low field transport

The velocity of carriers under the influence of an external electric filed is called drift velocity. At low fields this velocity is proportional to the applied electric field. The proportionality constant is called mobility μ. In an ideal case the drift velocity is simply the velocity the electron gains during the time when it is moving without scattering [2]. From the definition of mobility for electron we get

$$V_d = \mu E \quad 1.5$$

Hence mobility can be expressed as

$$\mu = \frac{e\tau sc}{m^*} \quad 1.6$$

Mobility has an inverse dependence with carrier mass.

1.2.2 High field transport

In most semiconductor devices the electronic transport is dominated by the high field transport, which occurs under strong electric fields. At very high electric field the electrons temperature increases and can be much higher than the lattice temperature. The

extra energy comes from the electric field. Also the drift velocities can be much higher. The velocity field relations are no longer linear and require complex numerical methods for their description. This high field velocity tends to saturate. Typically the velocity saturates at a value of 10^7 cm/s in nearly all semiconductors.

1.3 Optical absorption in semiconductors

In order for a semiconductor to be used for optoelectronic applications some property needs to be affected by radiation. The most commonly observed property is the generation of electron hole pairs due to incident radiation commonly known as "The Photoelectric Effect". This photoelectric generation can be measured as photocurrent using a properly designed external circuit. When radiation is incident on a semiconductor it imparts its energy to an electron. This process is known as absorption of a photon. For the electron to make a transition from the valence band to the conduction band the energy of the photon has to be equal or greater than the band-gap of the semiconductor. Photon absorption is strongest when the electron makes a direct transition into the conduction band. This is only possible in direct band-gap semiconductors.

The photon absorption for a particular wavelength is dependent on a parameter called the absorption co-efficient. This parameter indicates how strongly or weakly a photon is absorbed in the material and determines the number of electron hole pairs generated. In case of indirect band semiconductor materials an electron generation can only occur if a phonon participates in the interaction. The absorption co-efficient for these materials is hence a factor if 100 lower than direct co-efficient. The absorption co-efficient is expressed in cm^{-1}. It can also be expressed as a measure of how deep the light

penetrates into the material for a particular wavelength. Its value is zero above a particular wavelength known as the cut-off wavelength, in microns given by

$$\lambda c = \frac{hc}{Eg} \qquad 1.7$$

Direct band semiconductors show very strong absorption near the band edges whereas indirect band semiconductors have weaker absorption near the band edges.

1.4 Photoconductors

In layman's terms the primary function of a photodetector is to generate e-h pairs in response to incident radiation. This generation is measured using an external circuit in terms of photocurrent. In its simplest form a photodetector is a lab of a photosensitive semiconductor with contacts at the two ends. Other types of photodetectors include the p-i-n photodetector and the Avalanche photodetector. A photodetector, which consists only of a slab of intrinsic semiconductor with contacts, is called a photoconductor. We have used this configuration for our research. Incident radiation on the intrinsic region generates e-h pairs, which change the material' conductivity while the electric field causes the electrons and holes to move in opposite directions. Generally most research on photoconductors has assumed that light is incident on the bulk of the conductor, perpendicular to the applied electric field. This configuration is shown in fig. 1.2 below.

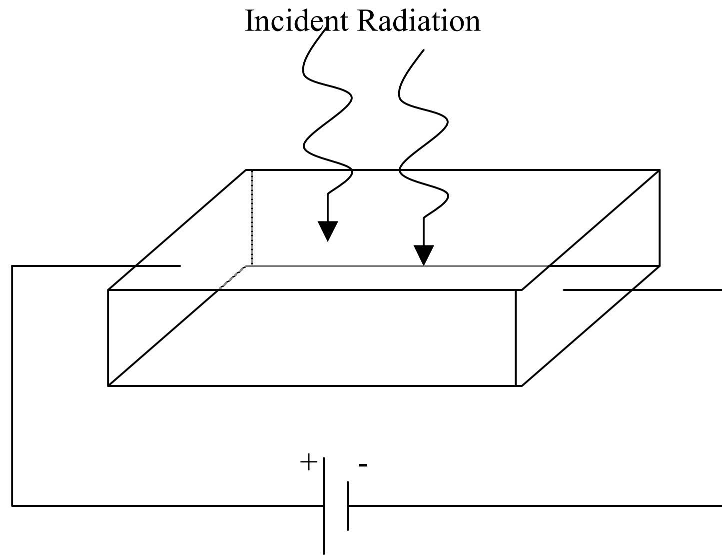

(a) Figure 1.2 (a) Geometry of a photoconductor

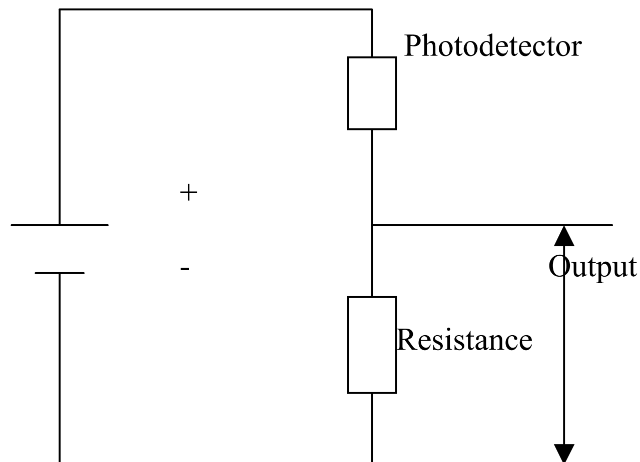

(b)Figure 1.2 (Continued) (b) Typical bias circuit for a photodetector

Another configuration that is possible is to have one of the contact electrodes transparent using contact material like SnO_2. The detector is then illuminated through the transparent electrode. The photogeneration is now along the applied field. This configuration is useful when studying thin film photoconductors, which are generally much thinner than

photoconductors fabricated from materials like silicon. The experimental setup that we have used for measurements on our samples uses this approach.

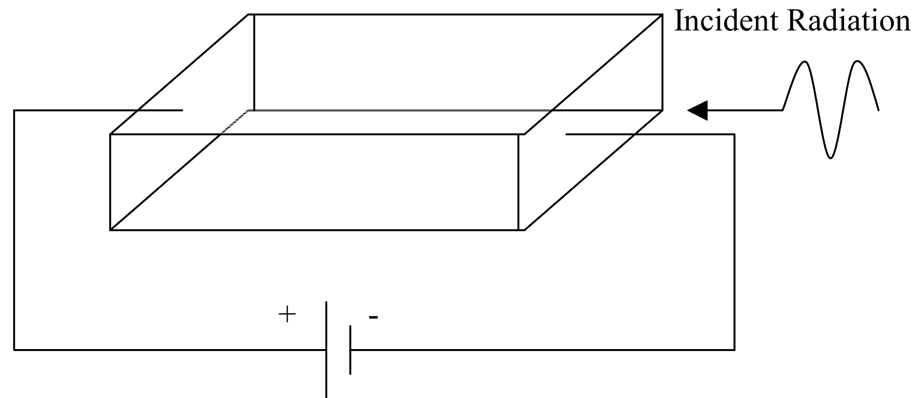

Figure 1.3 Schematic of bias circuit used for measurements

1.5 Compound semiconductors

Band transitions in indirect band semiconductors require in phonon collisions, whereas in direct band semiconductors they result in photon absorption or emission. Light emitting materials are used to manufacture LEDs or LASERs while light absorbing materials are used to manufacture photodetectors or solar cells. Silicon is the most widely used elemental semiconductor used in the semiconductor industry. But being an indirect band-gap semiconductor with poor radiative recombination it cannot be used to manufacture optoelectronic devices in crystalline form. Amorphous Silicon has been used to manufacture LEDs but the very high processing costs associated with it works against it[10].

Optoelectronic devices need to operate over a wide range of wavelengths depending upon their application. Silicon and Germanium impose a rigidty upon the incident radiation due to the inflexibility of their band-gaps. Band-gap modulation is one of the prime advantage a compound semiconductor provides over Silicon or Germanium.

These are generally composed of two or more elements, usually a metal and a non-metal. Electron mobilities five times greater than Silicon can be achieved for these films[6]. Important semiconductor materials exploited in optoelectronics are alloys like $Ga_xAl_{1-x}As$, which is lattice matched to GaAs substrates or $In_xGa_{1-x}As$, which is lattice matched to InP.

1.6 Mercuric iodide

Mercuric Iodide has generated interest due to its efficiency as a room temperature detector for high-energy radiation. The basic properties of this material are well suited for this application. The wide band-gap of 2.1eV at room temperature and its small temperature co-efficient result in a small thermal carrier generation over a wide temperature range[3]. The resistivity of pure crystals is approximately $10^{12}\Omega$-cm or higher. It has a density of 6.3g/cm^3, which results in a large absorption co-efficient. The photoelectric property is due to the large atomic numbers of the constituent elements (80 and 53)[3].

1.6.1 Crystal structure

The known polymorphic forms of mercuric iodide are: red α, yellow β and a metastable orange phase[4]. α-HgI_2 is tetragonal. Fig 1.4 shows the unit cell of α-HgI_2. Two Hg atoms are located at positions (0,0,0) and (1/2,1/2,1/2) and four I atoms at (0,1/2,u), (1/2,0,u), (0,1/2,1/2+u) and (1/2,0,1/2-u) with u=1.78Å . One mercury atom surrounded by four iodine atoms forms the co-ordination unit of the crystal. The slightly distorted tetrahedra are linked by the corners to form sheets parallel to the (001) plane. Each sheet consists of 3 layers of atoms (iodine-mercury-iodine). Mercury atoms occupy ¼ of the tetrahedrally coordinated voids of iodine sub-lattice in each sheet. Only weak

van der Waals bonding keeps the adjacent sheets together. The Hg-I distance within the tetrahedral is 2.783Å, whereas the shortest I-I distance is 4.142Å, which is found between neighboring layers of the tetrahedral. This structure is unique in that no other compound crystallizes in the same manner [4].

Table 1.1 Crystallographic data of α-HgI_2

Parameter	α-HgI_2
Lattice constant a (Å)	4.361
Lattice constant b (Å)	-
Lattice constant c (Å)	12.450
Molecules in unit cell	2

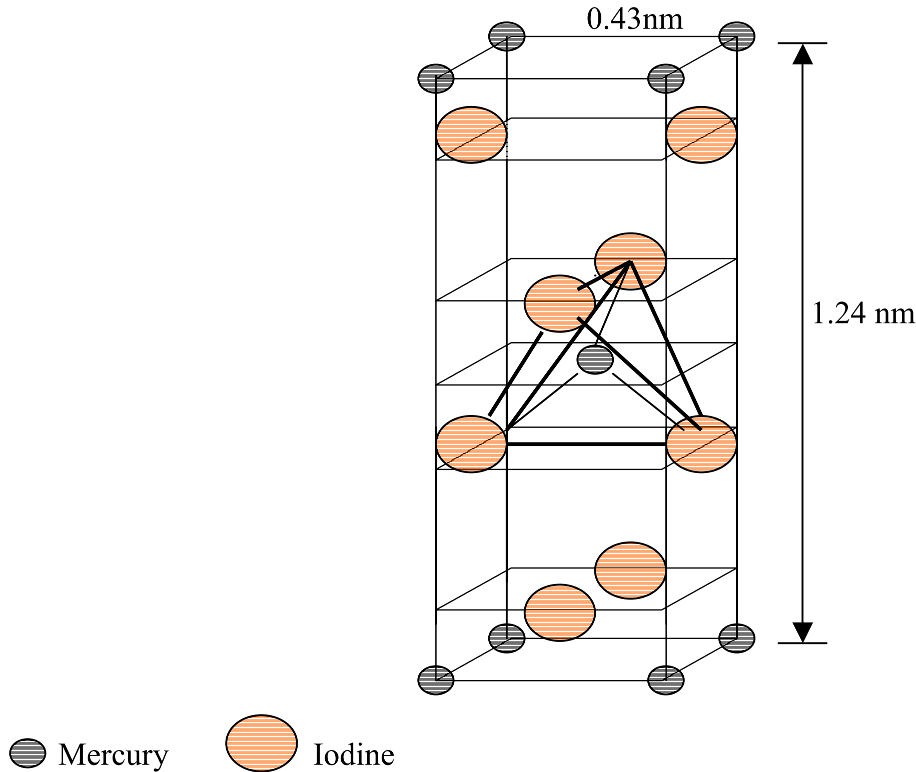

Figure 1.4 Elemental cell of tertragonal α-HgI_2

The tetragonal lattice shown in Fig.1.4 exists below 130°C. On heating above this temperature it transforms to the β phase. This phase has an orthorhombic lattice and has a band-gap of 2.5eV. If the β phase is cooled it transforms back into the α phase. This transformation is destructive in nature. Hence this material is generally used in operation below 130°C.

1.7 Objective of research

There are two basic objectives of our research. Polycrystalline mercuric iodide films are grown under varying growth conditions. High quantum efficiencies and low dark currents are desirable for these films. These parameters are strongly dependent upon the growth conditions of the films. An effort is made here to identify a set of optimum growth conditions for our films.

These films are being developed with x-ray applications in mind. Therefore ideally, an x-ray source should be the radiation source when performing optical measurements. But at this preliminary stage of the project visible light performs just as adequately as x-rays. Light of wavelengths 600nm and beyond is very weakly absorbed in the material and hence the carrier generation is very uniform. The generation profile is very similar to the profile for a low energy x-ray source. Other issues to be considered with x-ray sources are availability and hardware integration issues like acquiring the required peripherals.

Also, we have tried to calculate the transport parameters and the light absorption profile for our films with the help of simulations. A powerful semiconductor simulation tool named MEDICI^{tm} developed by Avanticorp is used for this purpose. In the following chapters we shall document the results of these simulations and attempt to comment on the growth conditions, transport and absorption parameters of these films.

1.8 Literature review

Lodewijk van den Berg et al. have fabricated single crystal detectors of 3mm thickness at Constellation technology Corporation[3]. The band-gap is measured as 2.13eV and the electron and hole mobilities are 100cm^2/Vs and 4cm^2/Vs. These measurements are further corroborated by McGregor et al. [5] who have been successful in fabricating single crystal detectors with a band-gap of 2.1eV and electron and hole mobilities of 100 and 4 cm^2/Vs respectively. Both groups observed high spectral resolution, low noise and room temperature operation capability. A common drawback observed by these and other groups is the current instability associated with the measurements. The current values fluctuate and it is also very difficult, nearly impossible

to reproduce a single set of readings. This can be attributed to the fact that mercuric iodide is wide band-gap semiconductor. Such current instabilities have been reported by Goorsky et al. [6] for other wide band-gap semiconductors like $Cd_{1-x}Zn_xTe$ and GaAs. Schlesinger et al. [7] have attempted to study this current instability and have reported that holding the sample under bias for a substantial amount of time reduces the instability and improves reproducibility of results.

For use in simulations certain electrical parameters like band-gap, mobility, absorption co-efficients etc. have been obtained from the literature. The absorption co-efficients have been obtained from two sources namely, Bube [8] and Schlesinger [9]. Comparitive analysis of this data leads us to believe that the quality of the Schlesinger material is much better than the material used by Bube. Mercuric iodide is expected to be transparent to incident radiation beyond 2.1eV. But the Bube samples show measurable response beyond 2.13eV as well. This is attributed to the fact that secondary phases with a lower band-gap exist which cause radiation to be absorbed beyond the expected value of 2.1eV. The Schlesinger values for absorption co-efficient drop off much more rapidly than the Bube values beyond the cut-off wavelength. This leads us to believe that the Schlesinger material is of better quality than the Bube material because it performs much closer to the expected theoretical performance.

CHAPTER 2

MEASUREMENTS ON POLYCRYSTALLINE FILMS

Response to light is an important tool in studying the electronic properties of H_gI_2. Both single crystal and polycrystalline films were evaluated as part of this research. The single crystal films are assumed to be with very low impurity concentration and defect densities. The I-V and Spectral response measurements on single crystal films were used as ideal cases. For the following measurements a tungsten-halogen lamp and an Oriel 1/4m monochromator were used. A focusing lens was used to concentrate the incident light onto a region smaller than the average polycrystalline sample size $0.1cm^2$. The measurements were recorded using the LabView^{tm} data-logging program.

An incident flux of $1e+15/cm^2$-sec for all wavelengths was used for the measurements. Bias orientation is with respect to the polarity of the illuminated electrode i.e. the front contact, which is also the growth surface for the films. It is observed that the signal obtained for –Ve bias is much greater than the signal obtained for +Ve bias at peak response wavelength. This is assumed to be due to the better transport properties for electrons, which have to travel the entire width of the sample under –Ve bias condition. The peak response wavelength range for both single crystal and polycrystalline films is between 570nm and 590nm. This corresponds approximately to a band-gap of 2.13eV, which is verifiable both by simulations, discussed later and by the experimental data discussed further on in the chapter. Dark I-V, Light I-V and Spectral Response were

measured for each sample. These measurements when correlated with the simulations give us an idea of the film properties, namely quality and transport properties.

2.1 Film structure and layout

The thickness of the thin films is in the range of 50-600μm. One of the objectives of this research is to prove that it is possible to grow polycrystalline films, which though much thinner than single crystal films can perform equally well. To meet this objective the parameters of measurements performed on the thin films are exactly the same as those performed on the single crystal samples. The same light and power sources are used for both sets of measurements.

The layout of a thin film is as shown in the figure below. Every thin film is grown on a film of SnO_2, which is deposited on glass. The film is 2.5cm in diameter.

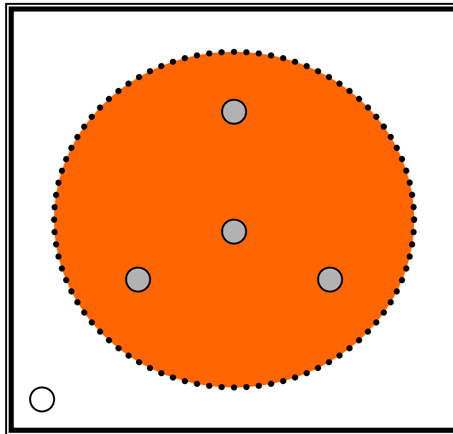

Figure 2.1 Layout of a typical polycrystalline film

Palladium contacts are then sputtered onto the film through a mask. The contact size is 0.1cm^2. The deposition rate and the source temperature for every individual film are kept constant. The substrate temperature is constant for some films while it is gradually increased over a period of time for others. It is observed that gradual increase of substrate temperature results in smaller grain size for films. By controlling the

deposition time, thickness of the films is varied. The deposition properties of the films are compared below.

Table 2.1 Deposition parameters

Sample	Tsrc(°C)	Tsub(°C)	Thickness(μm)	Deposition Rate(μm/hr)
9-5-02	70	5, 35	238.79	34.11
9-9-02	70	5, 40	203.22	29.03
9-11-02	70	5, 40	224.25	32.064
9-13-02	70	5, 35	211.56	30.22
9-17-02	70	5, 35	199.01	28.43
9-19-02	80	5, 40	243.11	51.72
9-27-02	80	5, 40	250.1	62.52
10-1-02	70, 80	5, 35, 50	151.18	37.79
10-2-02	70, 80	5, 50	162.17	32.43
10-3-02	70, 80	5, 35, 50	290.13	48.35
10-4-02	70, 80	5, 35, 50	199.13	36.2
10-8-02	70, 80	5, 35	230.92	41.98

2.2 Optical measurements

Spectral response, light and dark I-V measurements were performed on every sample. For films # 09-05-02 and beyond a new mask was used when sputtering the palladium back contacts. 7 samples were contacted instead of 4 for the previous films.

Since more surface area of the film is now covered this helps us in better studying the uniformity of the photoresponse.

Table 2.2 List of peak quantum efficiencies @ -50V

Film #	Sample #						
	1	2	3	4	5	6	7
9-5-02	0.65	0.49	0.59	-	0.45	-	-
9-9-02	0.9	0.4	-	0.72	0.85	0.70	0.42
9-11-02	0.48	0.51	0.46	0.5	0.49	-	0.42
9-13-02	0.59	0.70	-	0.71	-	-	0.59
9-17-02	-	-	0.71	-	0.59	0.97	0.47
9-19-02	0.25	-	0.23	0.27	0.43	-	0.21
9-27-02	0.39	0.33	0.5	-	0.5	0.37	0.36
10-1-02	0.70	0.62	0.27	0.4	0.75	-	0.51
10-2-02	0.68	0.61	-	0.78	0.62	0.61	0.65
10-3-02	0.48	0.38	0.57	0.40	0.63	-	0.60
10-4-02	0.45	0.3	0.56	-	0.57	-	-
10-8-02	0.48	0.52	-	0.61	0.48	-	0.5

Table 2.3 List of peak dark currents @ -50V

Film #	I_d(nA)						
	1	2	3	4	5	6	7
9-5-02	22	9	20	-	14	-	-
9-9-02	16.7	13	-	14.2	14	15.5	19
9-11-02	110	29	110	21	39	-	100
9-13-02	12	36	-	24	-	-	4.5
9-17-02	20	-	27	-	12	31	14
9-19-02	19	-	6	9	30.7	-	4.4
9-27-02	44	40	16	23	42	-	-
10-1-02	40	33.3	17.2	53	74	-	21
10-2-02	41	64	-	55	69	32	84
10-3-02	12	240	75	110	41	-	38.4
10-4-02	69	150	110	-	87	-	750
10-8-02	200	95	-	110	210	-	150

On studying the above tables we can find that almost all samples show fairly good quantum efficiencies. We use two performance related parameters, namely uniformity of performance and low dark currents to differentiate between a good and an average quality sample. The long-term objective of this project is to grow films for larger surface area medical imaging applications. For such applications it is very important that the

photoresponse at every point on the film be uniform as the output from a number of points on the film is collated to form the final image.

From this standpoint, films # 9-11-02, 10-2-02, 10-3-02 and 10-8-02 stand out as better films from the list above. Among these, 10-2-02 stands out as the best film. The quantum efficiencies for this film range from 0.61 to 0.78 with 6 out of the 7 samples on the film showing measurable photoresponse. What make this film the best though are the moderate dark current values associated with the samples ranging from 32nA for sample #6 to 84nA for sample #7. The thickness of this sample is 167.1µm, which makes it ideal for radiation detection applications.

In the following chapter we shall document in detail the film photoresponse simulations using MEDICI^{tm}, which help us determine the transport parameters and absorption profile of the light for the individual films. The simulations also help us to verify our conclusions regarding the selection of film # 10-02-02 as the best performing film of the lot.

CHAPTER 3

POLYCRYSTALLINE FILM SIMULATION

An attempt has been made by us to simulate the behavior of polycrystalline films using MEDICI^{tm}. This chapter documents the simulations and their outputs. A detailed explanation of the working of MEDICI^{tm} along with a sample program is available in the appendix. As explained in previous chapters the parameters of interest are the spectral response and the light and dark I-V characteristics. These parameters are simulated and compared with the measurements. The objective of these simulations is to estimate the transport properties and absorption data for each film.

3.1 Film #05-08-02

Table 3.1 Deposition parameters of film #05-08-02

Deposition profile	Single step
Substrate temp (°C)	40
Source temp (°C)	70
Estimated thickness (μm)	585.39
Deposition rate (μm/hr)	31.64

The deposition parameters for this film are shown in the table above. The film is deposited using the single step process. The estimated thickness of the film is 585.39μm. The measurements and simulations are shown in the plots below.

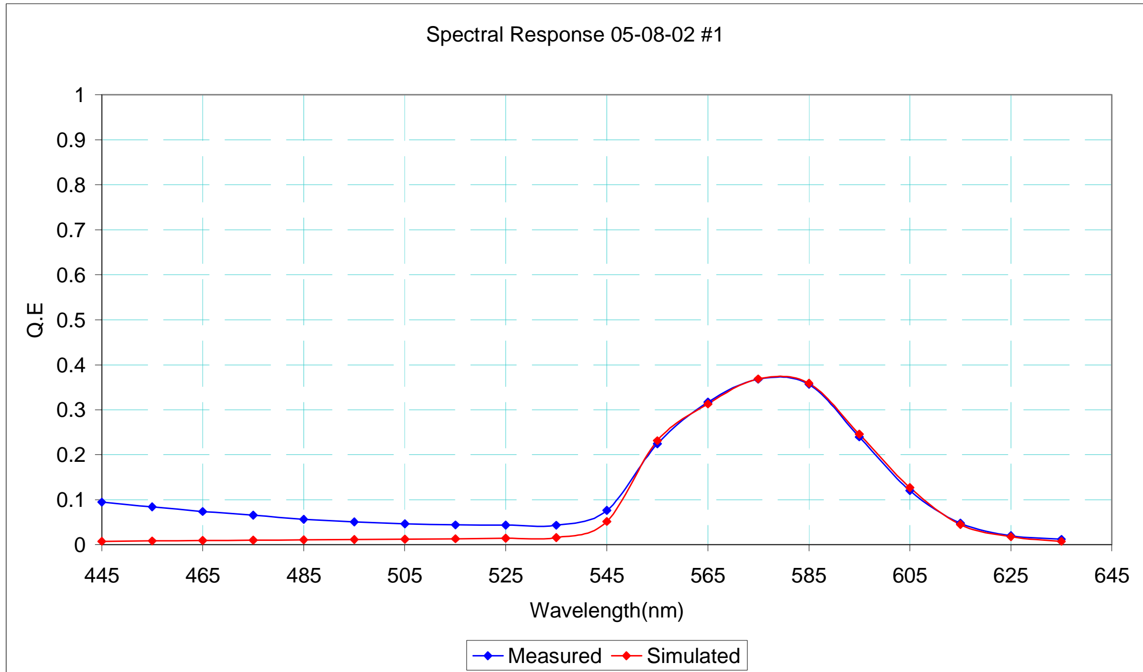

Figure 3.1 #05-08-02 Spectral response @ -50V

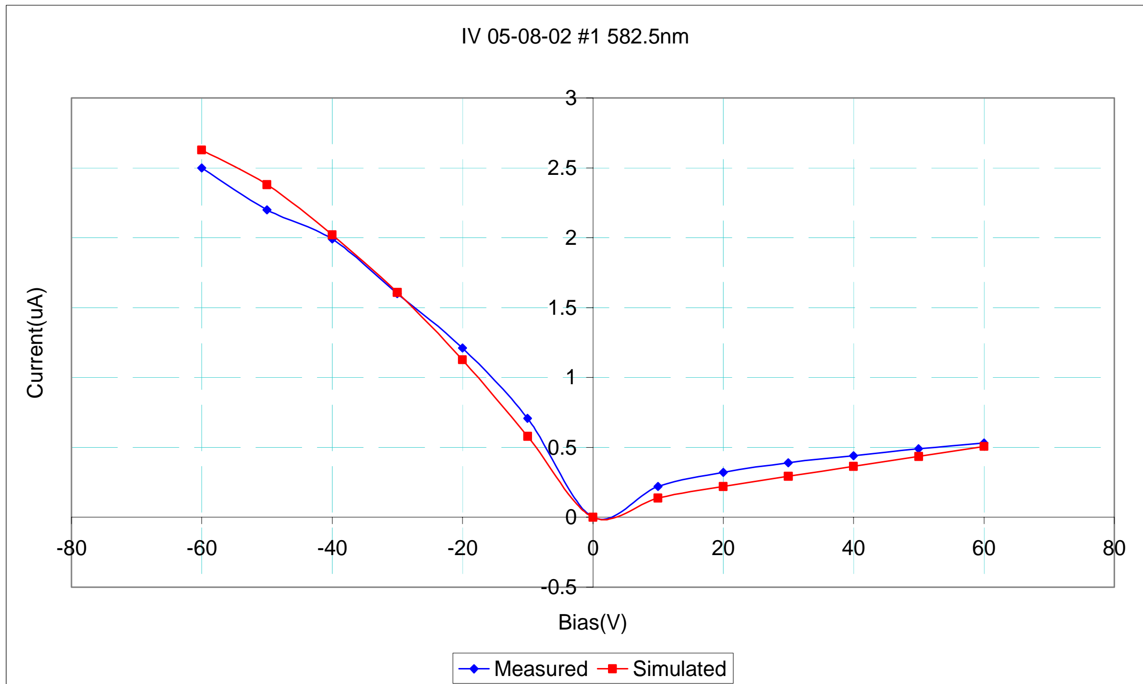

Figure 3.2 #05-08-02 Light I-V characteristics @ 582.5nm

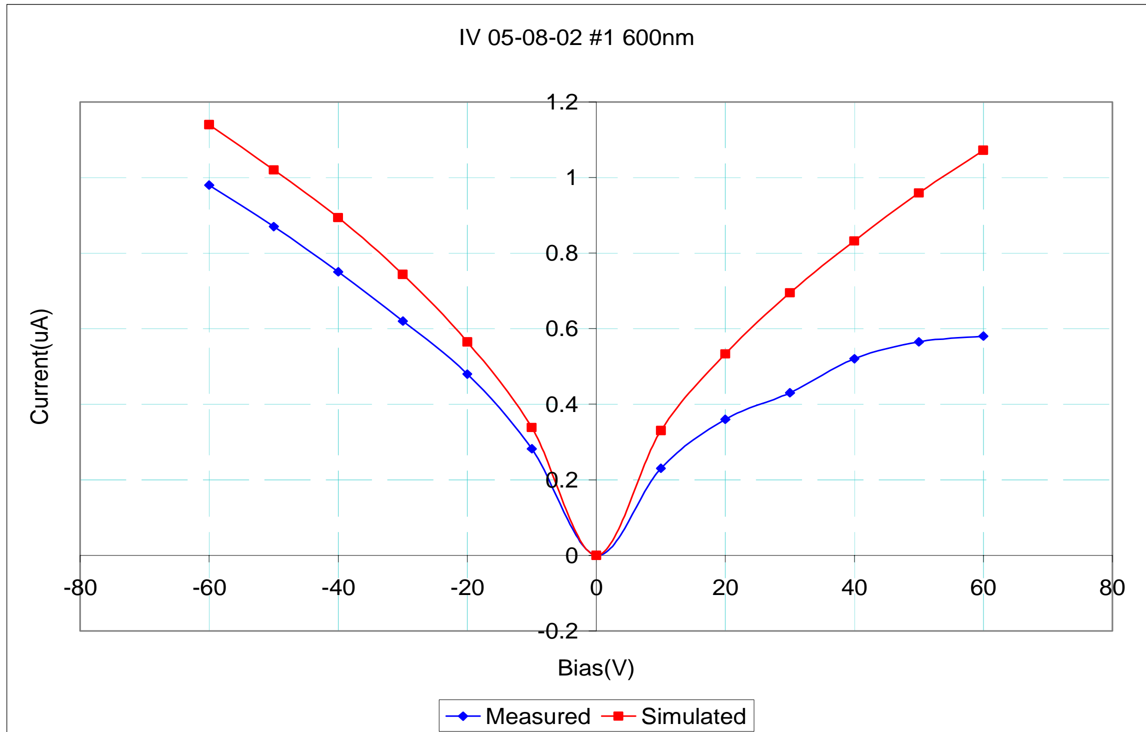

Figure 3.3 #05-08-02 Light I-V characteristics @ 600nm

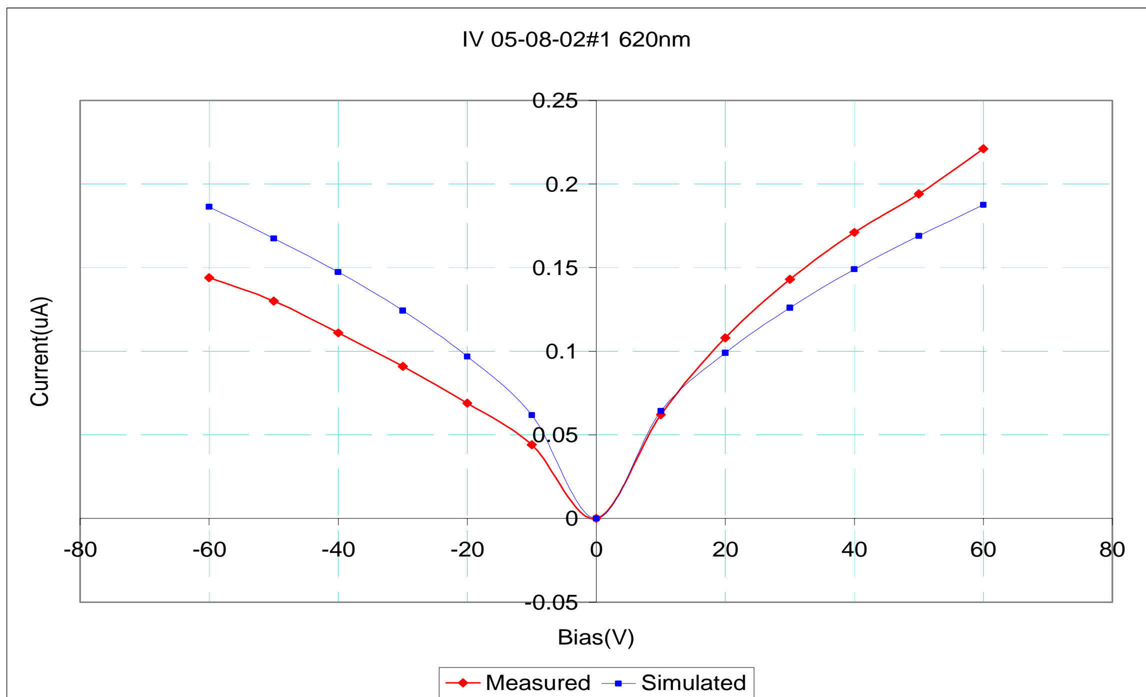

Figure 3.4 #05-08-02 Light I-V characteristics @ 620nm

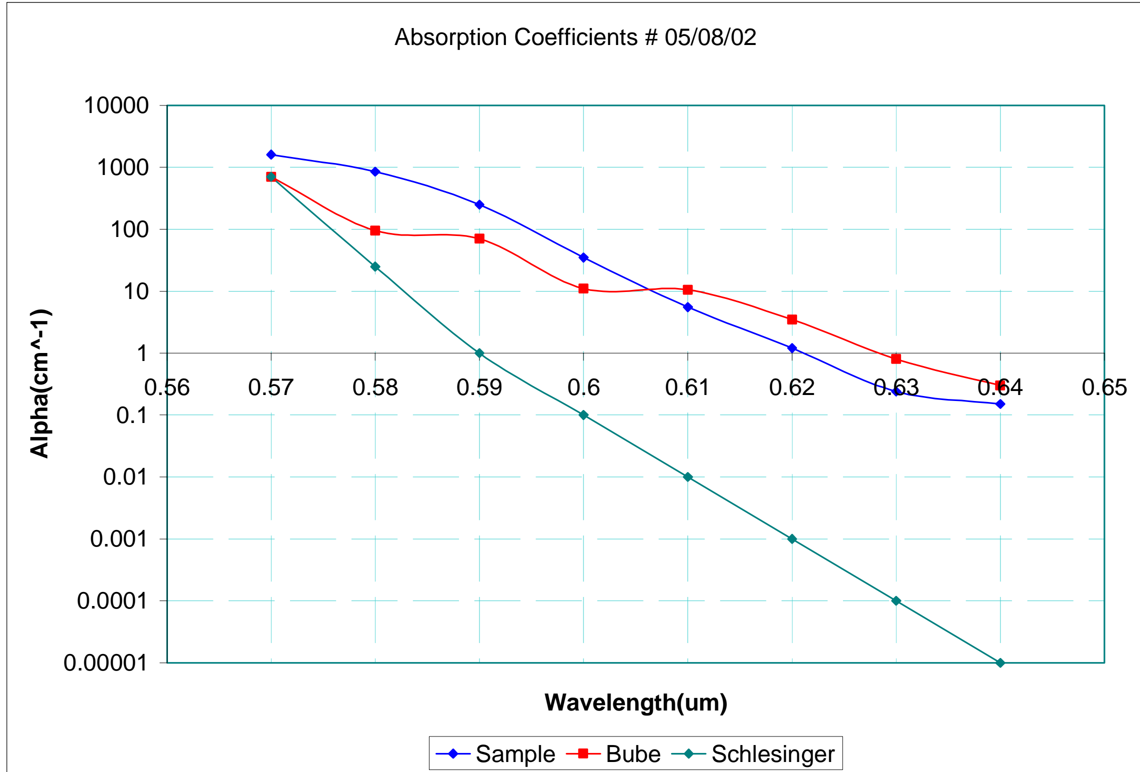

Figure 3.5 #05-08-02 Absorption data

A set of parameters is considered which gives the best possible congruence between the simulated and measured values for the I-V characteristics at 582.5nm and the spectral response at –50V bias. As a further means of checking the accuracy of parameters the I-V characteristics are further simulated at 600nm and 620nm and the output is compared to the measured values at these wavelengths. As seen above the simulated output very closely matches the measured output. Standard contact parameters were used for this simulation. The calculated parameters are shown in the tables below.

Table 3.2 Transport parameters for film #05-08-02

Carrier	$\mu\tau$ Product
Electron	4e-5
Hole	5e-8

Table 3.3 Absorption data for film #05-08-02

Wavelength (nm)	Absorption Coefficient (cm^{-1}) Bube	Absorption Coefficient (cm^{-1}) Schlesinger	Absorption Coefficient (cm^{-1}) Generated
570	700	700	1600
580	95	25	850
590	70	1	250
600	11	0.1	35
610	10.5	0.01	5.5
620	3.5	0.001	1.2
630	0.8	0.0001	0.24
640	0.3	0.00001	0.15

From the spectral response graph shown above we can see that the sample shows measurable photoresponse from 545nm. This indicates that light absorption is stronger at this wavelength onwards indicating a higher than expected value of absorption

coefficient. This belief is corroborated from fig.3.5 where we can see that the absorption co-effiecients between 570nm and 600nm are much higher than the literature values. This suggests that our films are of somewhat lower quality than single crystals.

Upon observing the measured light I-V curves at and 620nm we find that the response under +Ve bias is higher than the response under –ve bias. This phenomenon, we believe can be explained by studying the absorption profile for the light. At these wavelengths light is absorbed very close to the back contact. This results in increased collection for holes when the back contact is under –ve bias. At the same time electrons have to travel virtually the entire length of the sample i.e. nearly 600μm to be collected. Due to their high $\mu\tau$ product a substantial number of electrons are collected at the front contact. But when the biases are reversed i.e. the front contact is –ve and the back contact +Ve it is the holes that have to travel the entire sample length. This coupled with their very low $\mu\tau$ product results in high recombination for the holes. As a result the signal under –ve bias is diminished substantially. We cannot comment on the uniformity of performance of this film as only 2 of the 5 samples were responsive.

3.2 Film #09-17-02

Table 3.4 Deposition parameters for film #09-17-02

Deposition profile	Single step
Substrate temp in step 1 (°C)	45
Substrate temp in step 2 (°C)	35
Source temp (°C)	70
Eastimated thickness (°C)	199.01
Deposition rate (µm/hr)	31.642

The deposition parameters for this film are shown in the table above. The film is deposited using the two-step process. The estimated thickness of the film is 199.01µm. The measurements and simulations are shown in the plots below.

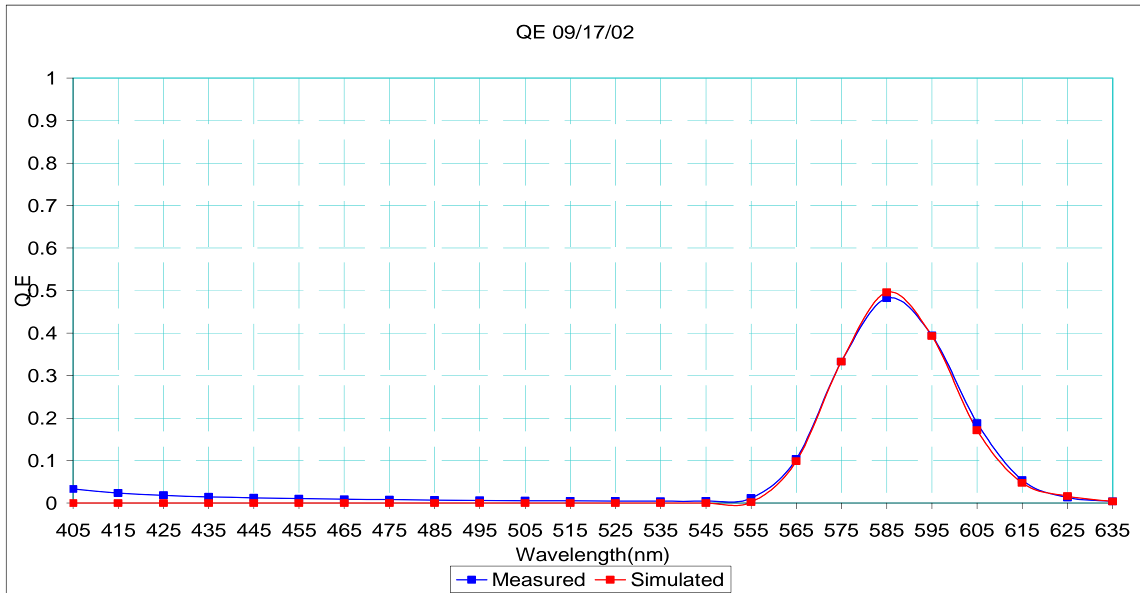

Figure 3.6 # 09-17-02 Spectral response @ -50V

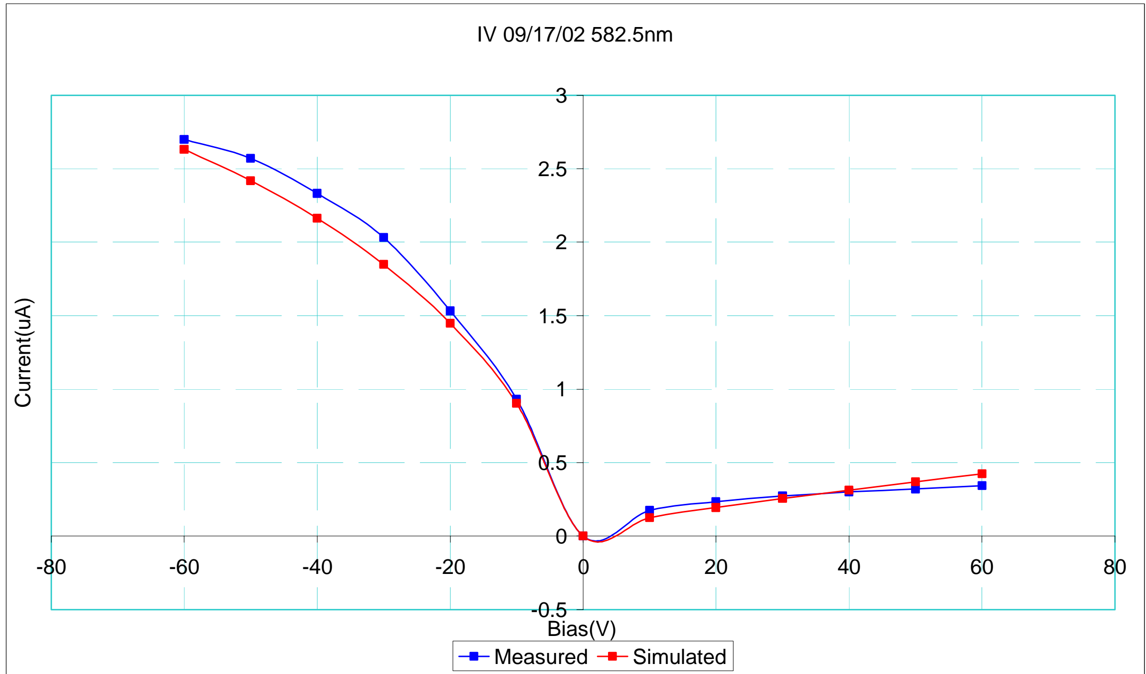

Figure 3.7 #09-17-02 Light I-V characteristics @ 582.5nm

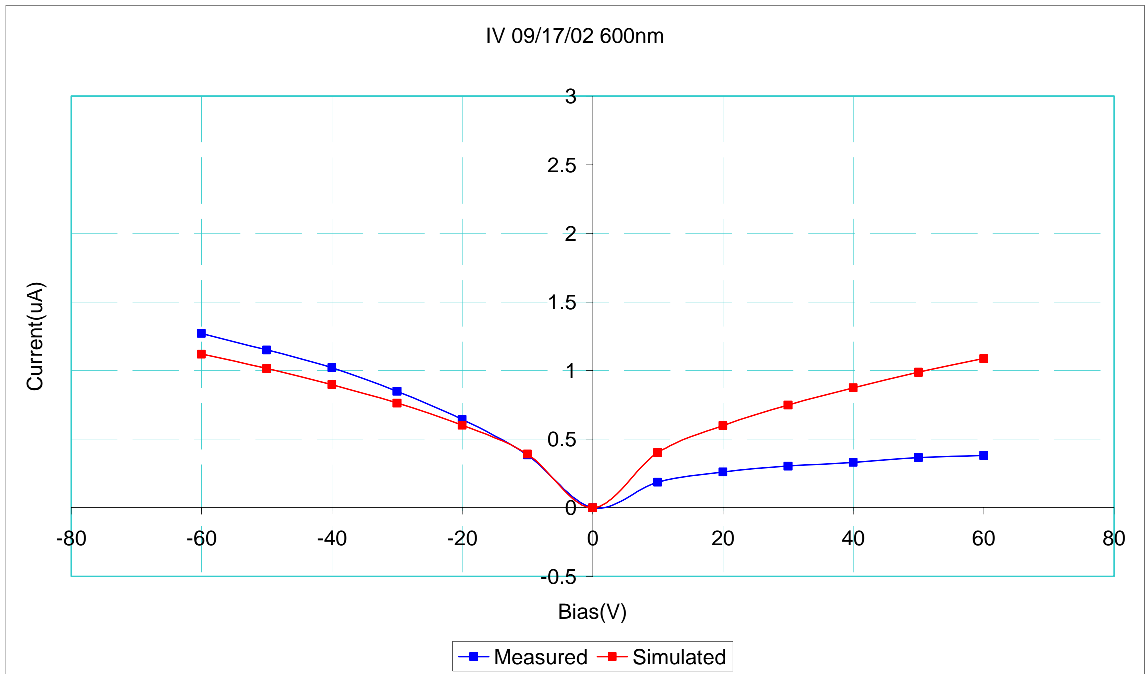

Figure 3.8 #09-17-02 Light I-V characteristics @ 600nm

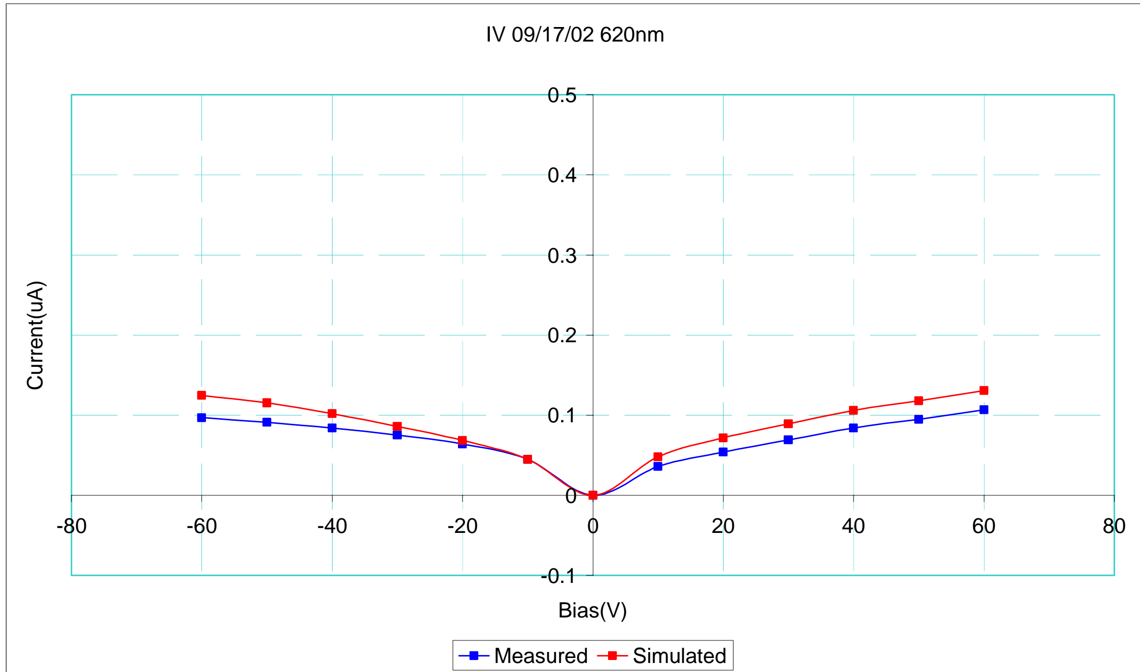

Figure 3.9 #09-17-02 Light I-V characteristics @ 620nm

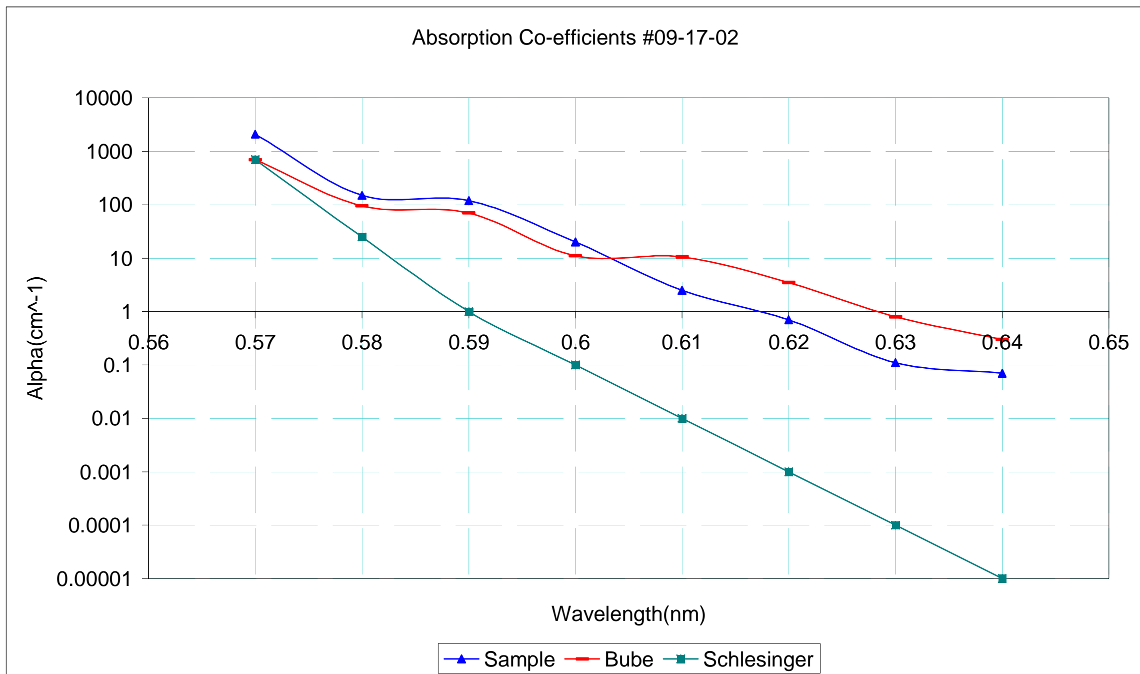

Figure 3.10 #09-17-02 Absorption data

From the plots above we can observe that the peak measured Q.E for the sample is 0.49. The peak response is observed at a wavelength of 585nm. The calculated parameters for the sample are shown in the tables below.

Table 3.5 Transport parameters for film #09-17-02

Carrier	$\mu\tau$ Product
Electron	1.435e-4
Hole	1.11e-8

Table 3.6 Absorption data for film #09-17-02

Wavelength (nm)	Absorption Coefficient (cm^{-1}) Bube	Absorption Coefficient (cm^{-1}) Schlesinger	Absorption Coefficient (cm^{-1}) Generated
570	700	700	2100
580	95	25	1500
590	70	1	120
600	11	0.1	20
610	10.5	0.01	2.5
620	3.5	0.001	0.7
630	0.8	0.0001	0.11
640	0.3	0.00001	0.07

A new mask was used when sputtering Palladium onto the film for contact deposition. 7 spots were deposited as compared to 5 for the earlier samples. All 7 samples were tested. 3 out of the 7 were found to be unresponsive. The peak quantum efficiencies and dark currents @ -50V are shown in the table below.

Table 3.7 Peak quantum efficiencies and dark currents for film #09-17-02

Sample no.	Peak Q.E @ -50V	Peak Dark Current @ -50V(nA)
1	Unresponsive	_
2	Unresponsive	_
3	0.71	27
4	Unresponsive	-
5	0.59	12
6	0.97	31
7	0.47	14

From the above table we can observe the large fluctuations of the peak quantum efficiencies for the samples. Non-uniformity in performance is detrimental to the use of these films in applications requiring large surface areas.

3.3 Film #10-02-02

Table 3.8 Deposition parameters for film #10-02-02

Deposition profile	Three step
Substrate temp in step 1 (°C)	5
Substrate temp in step 2 (°C)	35
Substrate temp in step 3 (°C)	50
Source temp in step 1 (°C)	70
Source temp in step 2 (°C)	80
Estimated thickness (°C)	162.17
Deposition rate (µm/hr)	32.43

The deposition parameters for the sample are shown in the table above. The estimated thickness of the sample is 162.17µm. This sample is one of the first deposited with the three-step process. The substrate temperature is maintained at 5°C for 15 min, and then finally stabilized at 50°C. The measurements and simulations for this sample are shown below.

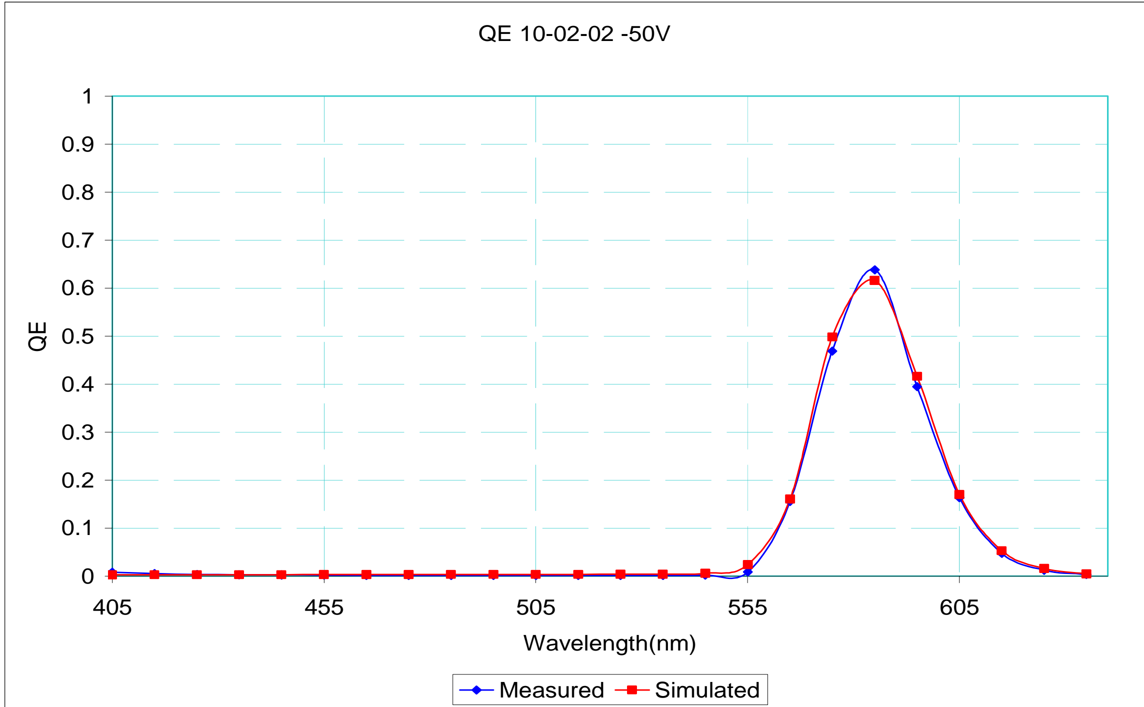

Figure.3.11 #10-02-02 Spectral response @ -50V

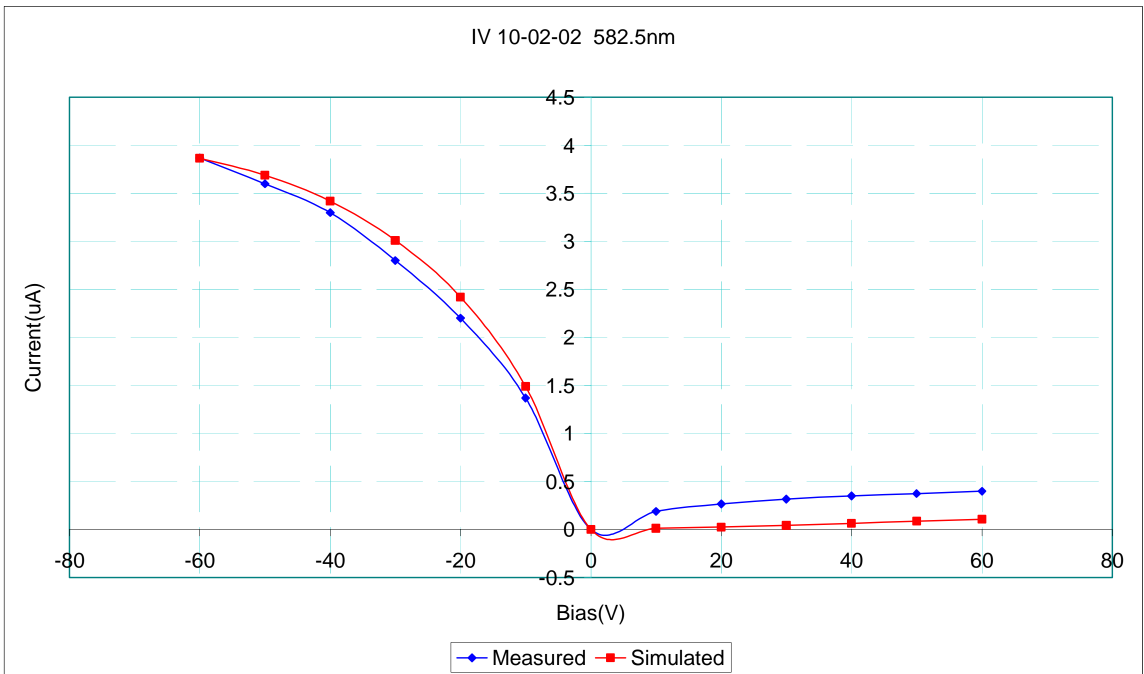

Figure 3.12 #10-02-02 Light I-V characteristics @ 582.5nm

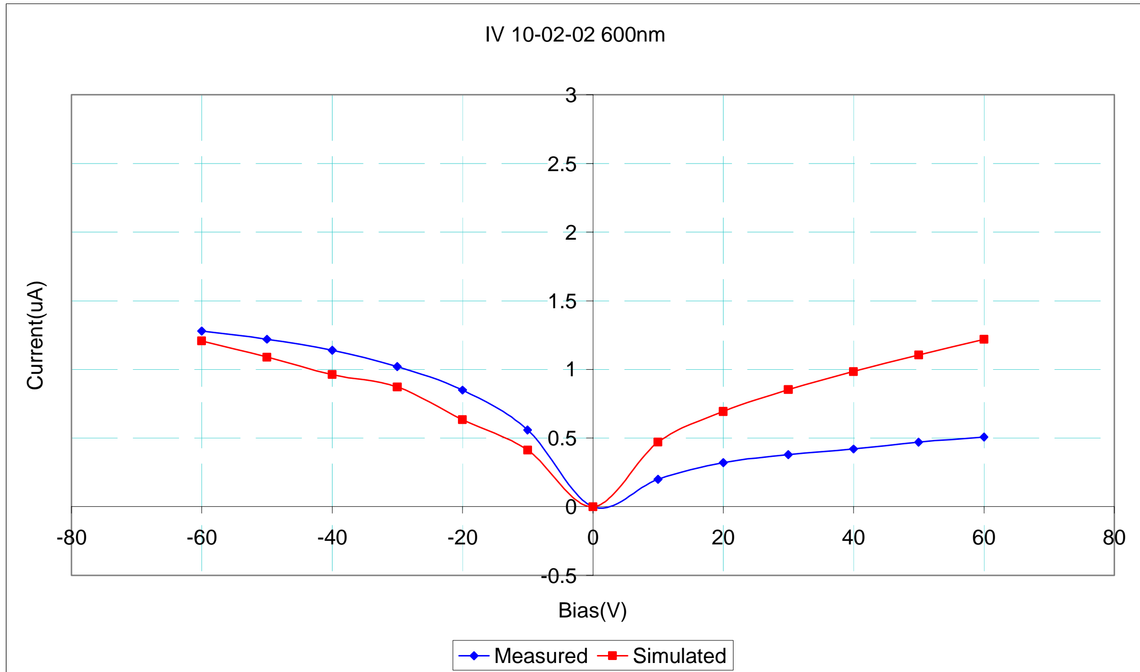

Figure 3.13 #10-02-02 Light I-V characteristics @ 600nm

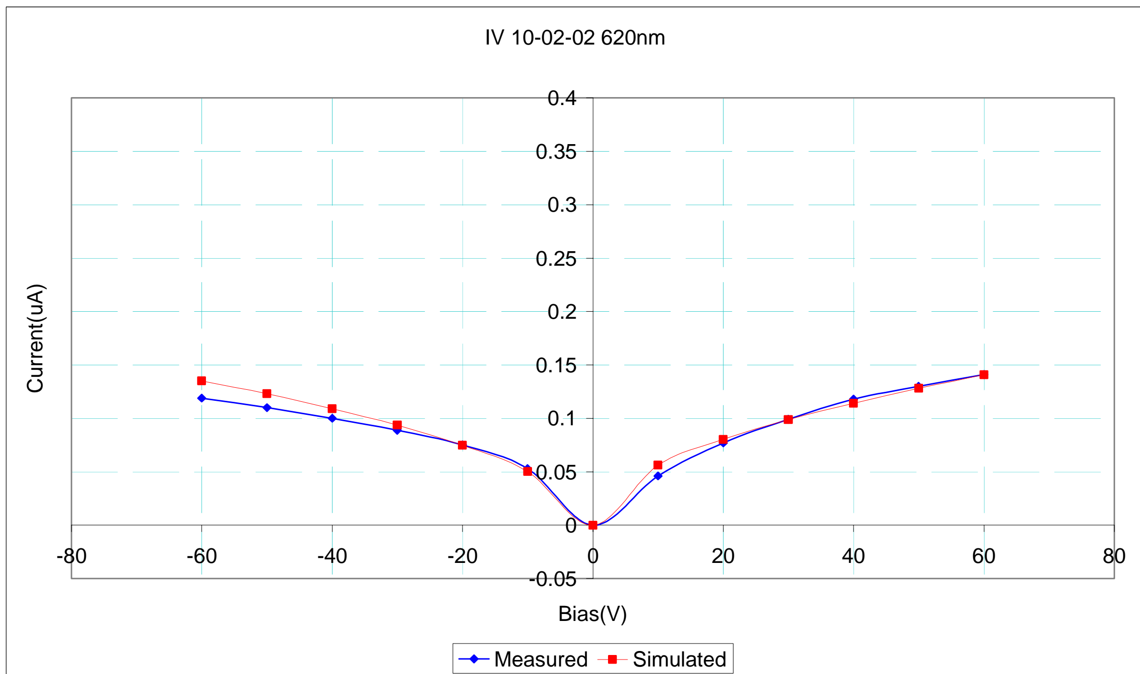

Figure 3.14 #10-02-02 Light I-V characteristics @ 620nm

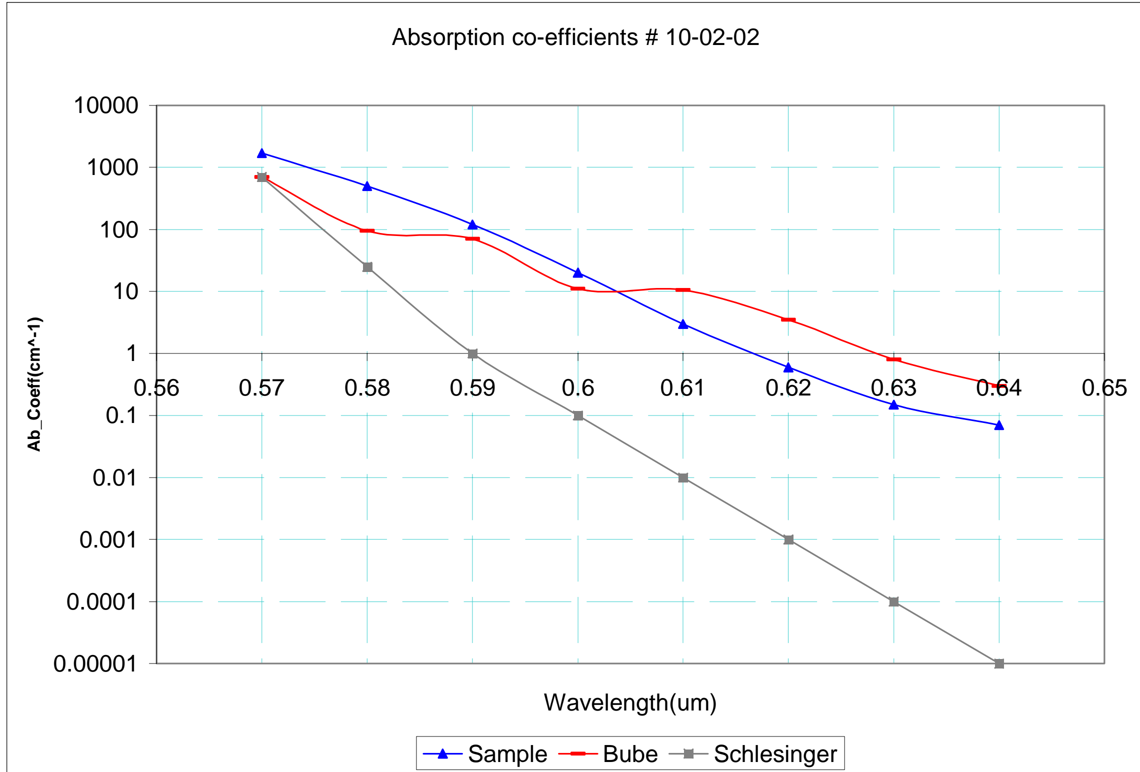

Figure 3.15 #10-02-02 Absorption data

From the plots above we can observe that the peak measured Q.E for the sample is 0.49. The peak response is observed at a wavelength of 585nm. The calculated parameters for the sample are shown in the tables below.

Table 3.9 Transport parameters for film #10-02-02

Carrier	μτ Product
Electron	1.2e-4
Hole	1.5e-9

Table 3.10 Absorption data for film #10-02-02

Wavelength (nm)	Absorption Coefficient (cm^{-1}) Bube	Absorption Coefficient (cm^{-1}) Schlesinger	Absorption Coefficient (cm^{-1}) Generated
570	700	700	1700
580	95	25	500
590	70	1	120
600	11	0.1	20
610	10.5	0.01	3
620	3.5	0.001	0.6
630	0.8	0.0001	0.15
640	0.3	0.00001	0.07

This film shows the most consistent response among all films measured yet. This is illustrated in the table below. 6 out of the 7 samples on this film show measurable response. This coupled with the low dark current values makes this one of the better performing film.

Table 3.11 Peak quantum efficiencies and dark currents for film #10-02-02

Sample no.	Peak Q.E @ -50V	Peak Dark Current @ -50V(nA)
1	0.68	41
2	0.61	64
3	Unresponsive	-
4	0.78	55
5	0.62	69
6	0.61	32
7	0.65	84

3.4 Film #10-03-02

Table 3.12 Deposition parameters for film #10-03-02

Deposition profile	Three step
Substrate temp in step 1 (°C)	5
Substrate temp in step 2 (°C)	35
Substrate temp in step 3 (°C)	50
Source temp in step 1 (°C)	70
Source temp in step 2 (°C)	80
Estimated thickness (°C)	290.13
Deposition rate (µm/hr)	48.35

The deposition parameters for the sample are shown in the table above. The estimated thickness of the sample is 290.17μm. The source and substrate temperatures have the same magnitudes as those for film # 10-02-02. The only variation is the duration of each temperature step. The substrate temperature is maintained at 5°C for 15 min, then at 35°C for 45 min and then final stabilized at 50°C. The source temperature is maintained at 70°C for 28 min and 80°C the rest of the way. The measurements and simulations for this sample are shown below.

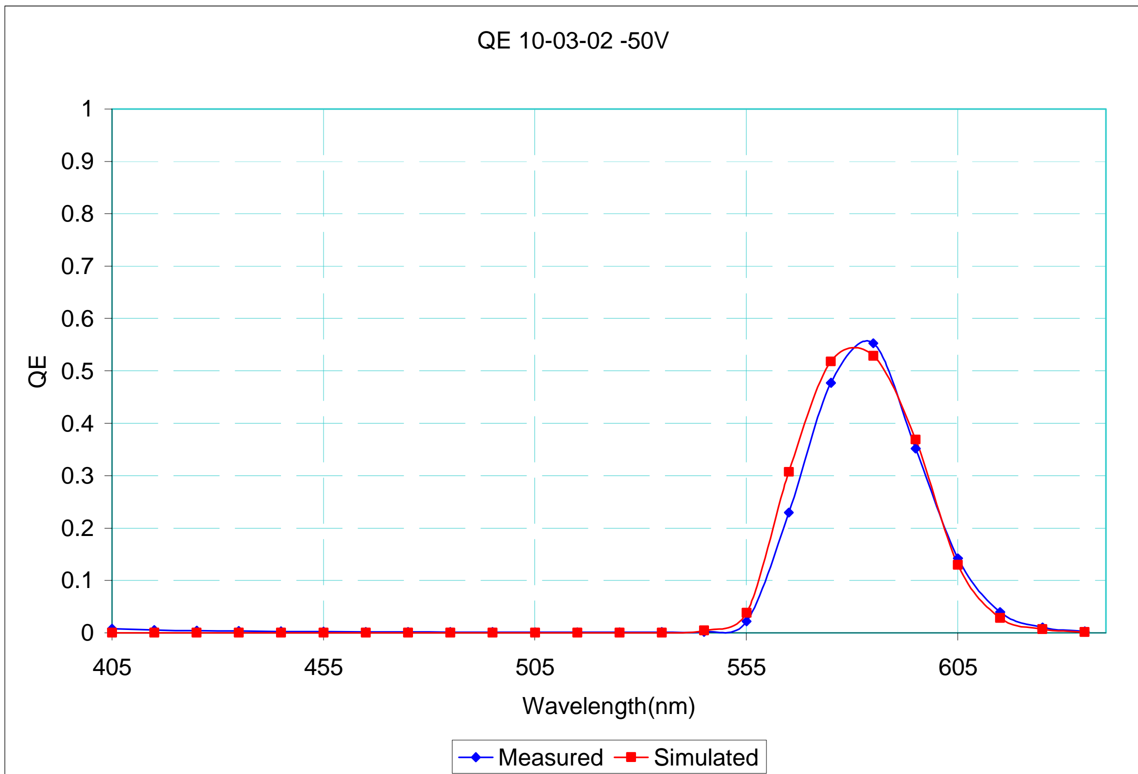

Figure 3.16 #10-03-02 Spectral response @ -50V

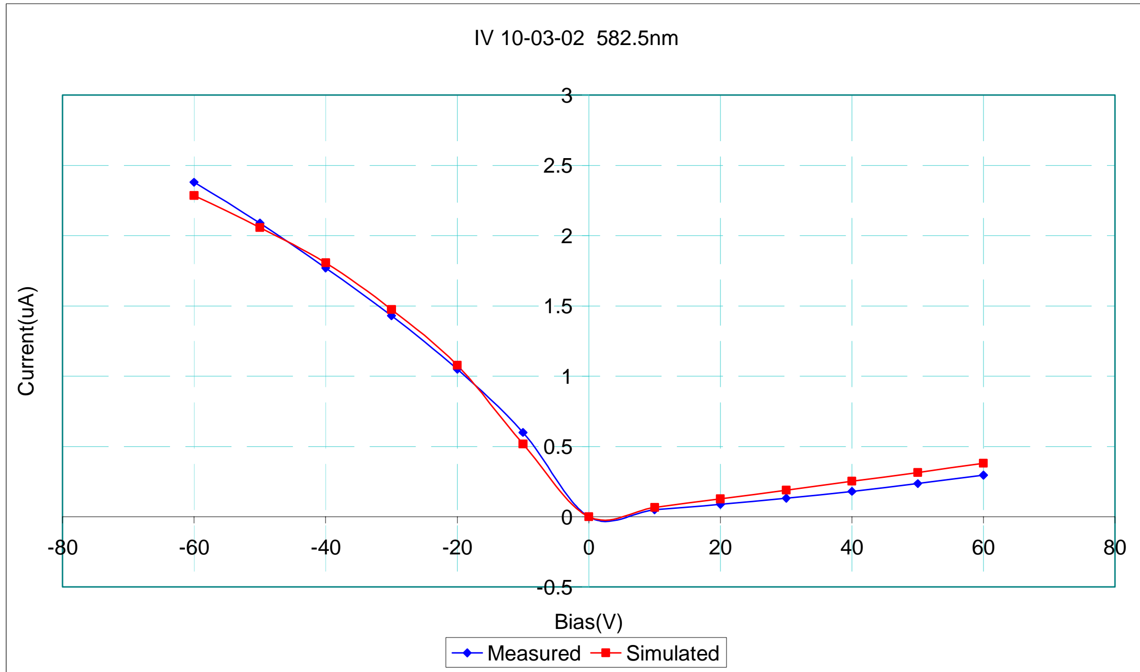

Figure 3.17 #10-03-02 Light I-V characteristics @ 582.5nm

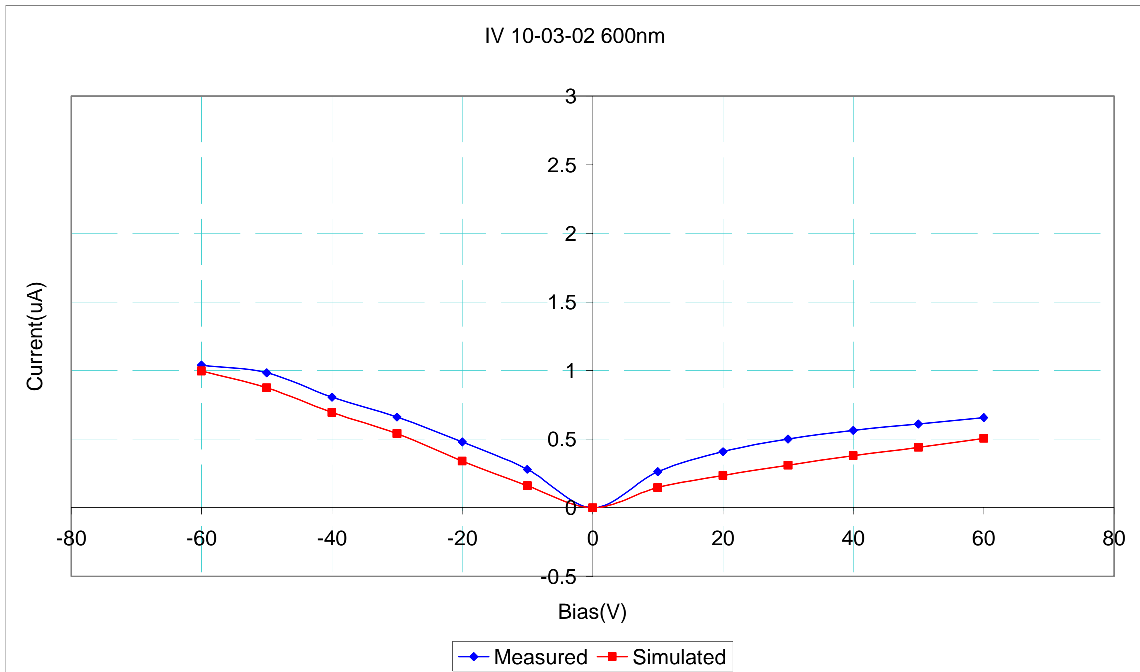

Figure 3.18 #10-03-02 Light I-V characteristics @ 600nm

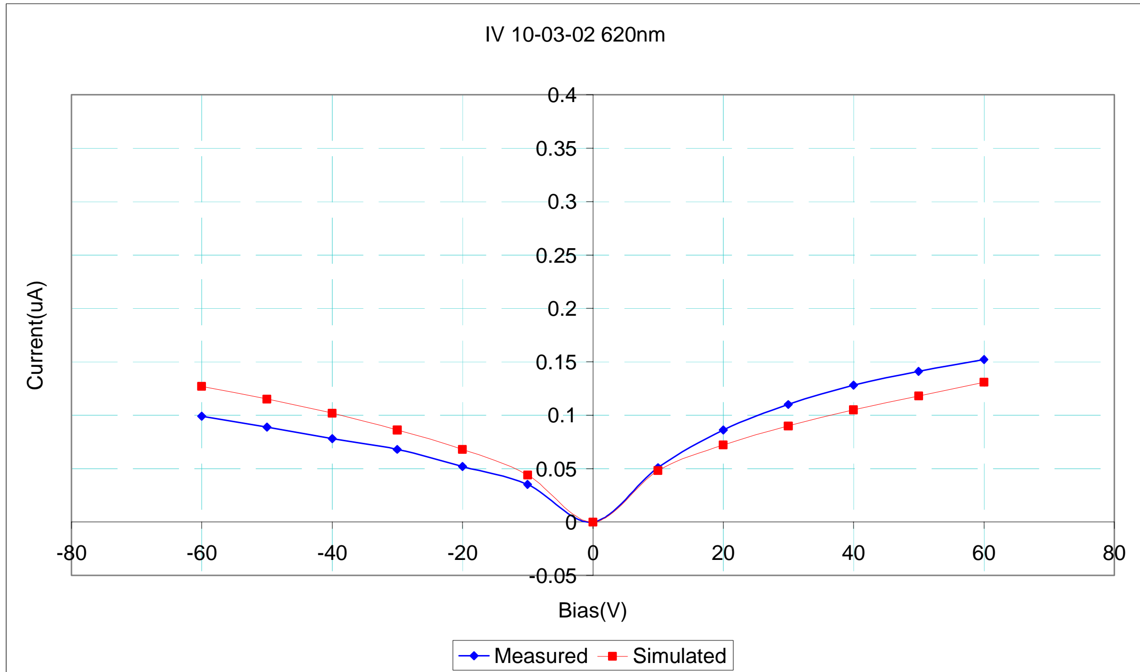

Figure 3.19 #10-03-02 Light I-V characteristics @ 620nm

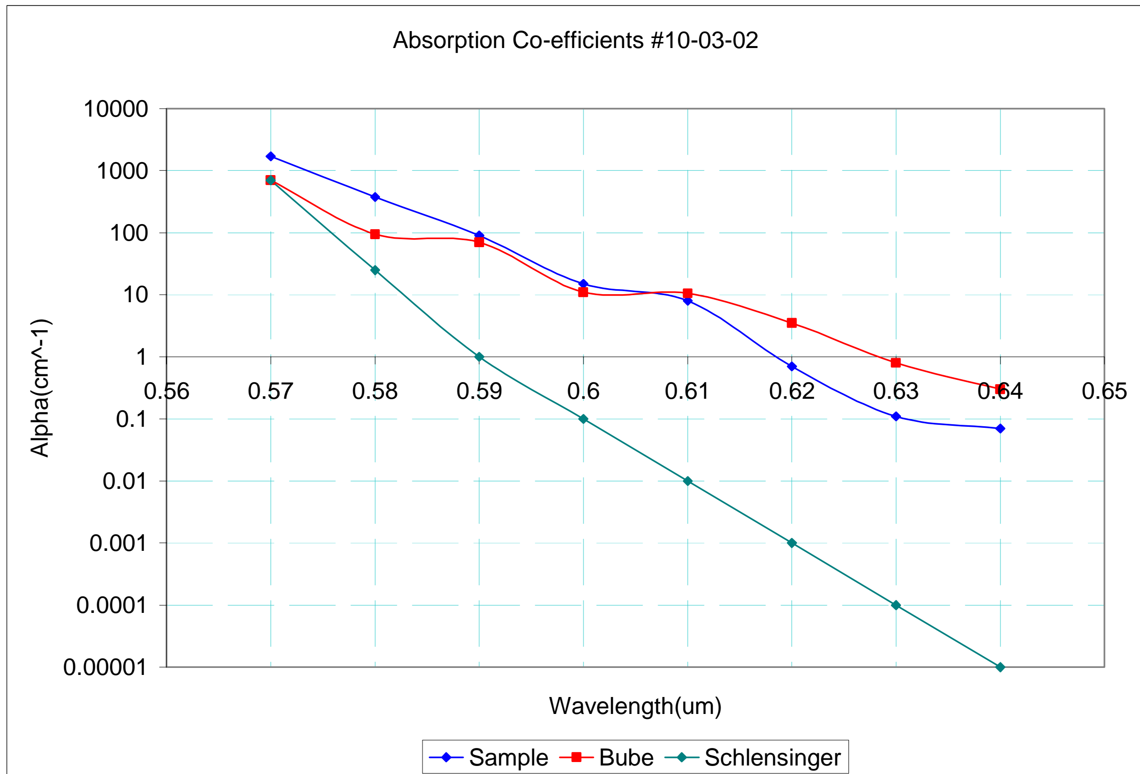

Figure 3.20 #10-03-02 Absorption data

From the plots above we can observe that the peak measured Q.E for the sample is 0.57. The peak response is observed at a wavelength of 582.5nm. The calculated parameters for the sample are shown in the tables below.

Table 3.13 Transport parameters for film #10-03-02

Carrier	$\mu\tau$ Product
Electron	1.025e-6
Hole	2.5e-10

Table 3.14 Absorption data for film #10-03-02

Wavelength (nm)	Absorption Coefficient (cm^{-1}) Bube	Absorption Coefficient (cm^{-1}) Schlesinger	Absorption Coefficient (cm^{-1}) Generated
570	700	700	1700
580	95	25	375
590	70	1	90
600	11	0.1	15
610	10.5	0.01	8
620	3.5	0.001	0.7
630	0.8	0.0001	0.11
640	0.3	0.00001	0.07

The peak quantum efficiencies and peak dark currents for all samples on this film are shown in the table 3.15 below.

Table 3.15 Peak quantum efficiencies and dark currents for film #10-03-02

Sample no.	Peak Q.E @ -50V	Peak Dark Current @ -50V(nA)
1	0.48	13
2	0.38	240
3	0.57	75
4	0.40	110
5	0.63	41
6	Unresponsive	-
7	0.60	38.4

Quantum efficiencies as high as 0.63 are obtained for this film. Also 6 out of 7 samples are responsive. Sample # 2 has a peak quantum efficiency of 0.38 while the peak quantum efficiency for sample # 5 is 0.63. This indicates non-uniform photoresponse over the entire film. Dark currents as high as 240nA are measured for this film. The following section documents the comparison of these films on the basis of measured and simulated parameters.

3.5 Qualitative analysis and conclusions

In chapter.2 we have documented the optical measurements performed on polycrystalline HgI_2 films. From preliminary conclusions based on the measurements 4 of the better performing films were selected for further analysis using simulations. The

simulations when grouped together with the optical measurements help us analyze the film quality on the basis of performance.

Films are compared on the basis of measured parameters like peak quantum efficiency and peak dark currents and simulated parameters like transport properties and absorption co-efficients. These comparisons are documented in Table 3.16 and Fig 3.21 below.

Table 3.16 Comparison of generated and measured parameters

	# 05-08-02	# 09-17-02	#10-02-02	#10-03-02
Peak quantum efficiency	0.38	0.71	0.68	0.62
Peak dark currents	-	22	78	240
Electron $\mu\tau$ product	6e-5	1.5e-4	1.25e-4	1e-6
Hole $\mu\tau$ product	6e-8	1e-8	1.5e-9	2e-10

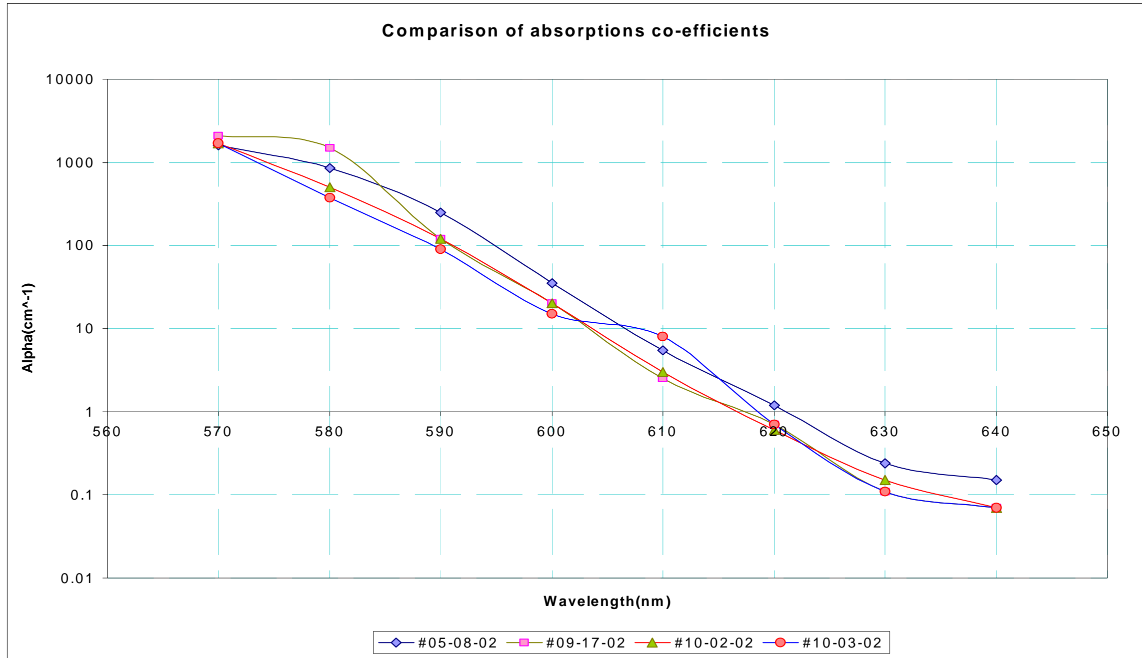

Figure 3.21 Comparison of absorption properties generated from simulations

From the above table and plot we can see that the best quantum efficiencies coupled with the lowest dark currents are exhibited by films # 09-17-02 and # 10-02-02. We can also see that the electron μτ product for these two films is the highest among the films simulated. However only 4 out of the 7 samples on film # 09-17-02 are responsive as compared to 6 for films # 10-02-02. The absorption co-efficients of # 10-02-02 show a uniform and orderly dependence on the wavelength without any kinks as seen in the absorption profile of other samples. This indicates good film quality. These factors when grouped together lead us to believe that film # 10-22-02 is the best film amongst all films grown yet.

CHAPTER 4

CONCLUSION

4.1 Conclusion

Several polycrystalline HgI_2 films were studied as part of this work. Optical measurements were performed on these films. The same experimental setup and measurement conditions are used for all samples. The preliminary comments on the film, deposition, quality and individual device performance were presented in Chapter 2. The peak quantum efficiency @ -50V bias and the peak dark current @ 50V along with the deposition parameters are documented. Quantum efficiencies between 0.4 and 0.7 are consistently obtained. Dark current values in the nano-amperes are also obtained indicating low leakage currents. Classification of a film as very good/good/bad is made on the basis of good and uniform photoresponse on all individual samples on the film and low dark currents. Based on the measurements we can conclude that films # 05-08-02, 09-17-02, 10-02-02 and 10-03-02 show the best performance. These films were selected for further analysis.

MEDICI^{tm} simulations were performed on these films. The light I-V characteristics and spectral response for each film were simulated. The obtained simulations were found to be consistent with the measurements. Transport parameters and light absorption profiles are known for single crystal films and can be obtained from literature. In the case of polycrystalline films these parameters, which are strongly

dependent on the deposition parameters are yet unknown. By comparing the simulations to the measurements we have obtained these parameters for the above-mentioned films. These simulations and their output are explained in Chapter 3.

Film # 10-02-02 generates the most interest from the 4 films selected. 6 out of the 7 samples on this film are responsive and show high and uniform quantum efficiencies ranging from 0.61 to 0.68. Sample #4 is the lone anomaly on this film showing a higher than expected quantum efficiency of 0.78. Also low dark current values ranging from 32nA to 84nA are measured for all samples. The $\mu\tau$ products for electrons and holes are 1.2e-4 and 1.5e-9. Also the light absorption profile for this film is uniform and does not show many kinks like the profiles for other films. These factors coupled together strengthen our belief that film # 10-02-02 is the best film studied yet. This film has been grown with the composite two-step process where both the substrate and source temperatures are increased in two steps. The thickness of this film is 162.17µm, which is ideal for radiation detector applications.

4.2 Future work

This research serves as an overview to the potential HgI_2 holds towards being a premier material in the development of large-area room temperature nuclear radiation detector. So far, the diameter of the polycrystalline films fabricated by us has been 2.5cm. The uniformity in performance, high quantum efficiency and low leakage current of these films instills confidence that large area imaging applications can be developed with this material.

We have been successful in identifying a set of growth parameters, which can result in good quality films. More films using those growth parameters will have to be

grown and characterized further to optimize the growth process. Also at present TEC-15 LOF glass is the substrate of choice for film growth. A variety of substrates could be tried to check if the performance of the films can be improved. Also, thus far visible light has been used in optical measurements on these films. The light source could be replaced with a gamma-ray source to test these films under conditions similar to their real life applications. Another issue that needs to be dealt with is the current instability associated with the measurements.

With a span of just 18 months we have managed to develop thin film devices, which are comparable and at times better in performance to single crystal HgI_2 detectors. This perhaps is the most compelling reason to continue this research at USF.

REFERENCES

1. www.public.asu.edu/~ntao1/ECE352/ECE04-11.ppt

2. S.M. Sze, *Physics of Semiconductor devices*, 2nd Edition, New York, Wiley-Interscience, 1999.

3. Lodewijk van den Berg et al., "*Mercuric Iodide X-Ray and Gamma Ray detectors for Astronomy*", www.contech.com.

4. M. Piechotka, "*Mercuric Iodide for room temperature radiation detectors. Synthesis, purification, crystal growth and defect formation*", Materials Science and Engineering, R18 I-98, Elsevier Science S.A, 1997.

5. D.S. McGregor et al., "Room temperature semiconductor radiation detectors".

6. M.S. Goorsky et al., "X-ray diffuse for evaluation of wide bandgap semiconductor nuclear detectors", Nuclear Instruments and Methods in Physics research A 380 (1996) 6-9.

7. B.A. Brunett et al., "Two-dimensional photocurrent mapping of mercuric-iodide detector crystals", Nuclear Instruments and Methods in Physics Research A 380 (1996) 70-75.

8. R.H. Bube, Phys. Rev. 106 (4) (1957) 703.

9. X. Bao, R. James, T. Schlesinger, Optical properties of red HgI_2, in: T. Schlesinger, R. James (Eds), Semiconductors and Semimetals, vol. 43, 1995, p. 493.

10. S. Wolf and R.N. Tauber, Silicon Processing for the VLSI Era, 2nd Edition, Lattice Press.

APPENDICES

Appendix I MEDICI^{tm}

MEDICI^{tm} is a powerful device simulation tool that can be used to simulate the behavior of optoelectronic and other semiconductor devices. It can predict characteristics like photogeneration, recombination, and carrier collection at arbitrary bias and wavelength conditions. It can solve Poisson's equation and Continuity equations for electrons and holes as well as for devices like photodetectors where current flow is single carrier dominated.

Physical models incorporated in MEDICI^{TM} include models for recombination, photogeneration, mobility, lifetime as well as Boltzmann and Fermi Dirac Statistics. Advanced application modules like Optical Device AAM are available. A non-uniform triangular grid is used in simulations. This grid divides the associated region in smaller triangular regions that are individually solved and the individual solutions are correlated to generate the final output. The grid can be refined dynamically during simulations based on parameters like doping or photogeneration. Thus greater simulation power can be allocated to regions of maximum activity while lesser resources are allocated to regions of lower activity.

The program begins with the title statement followed by the simulation mesh definition. Specifying the width of the region and then dividing it into smaller sub divisions by specifying the dimension of each sub division define the x component of the mesh.

Appendix I (continued)

The y component of the mesh is defined similarly using the depth of the region and sub division dimension. Since only one bulk semiconductor region is used for our device one mesh declaration for that region is enough to declare the mesh for the entire device. The device layout declaration is completed by defining the contact positions with respect to the bulk semiconductor. This can be done using the electrode statement. This statement only assigns a name to the electrode and assigns it a position in the device. Contact properties are declared later. MEDICI^{tm} has a material library where semiconductors like Si, Ge, SiC, GaAs etc are declared and stored along with their parameters. HgI_2 does not come under this category of stored materials. To declare a material not present in the material library MEDICI^{tm} provides the user with a material named semicond. The user defines these properties using the material statement. Mobilities for the material can be defined using the mobility statement. Contact properties are defined next using the contact statement. The incident light source has been defined using the photogen statement with the raytrace argument. The location and the intensity of the light source in terms of the incident flux have to be specified. The absorption properties of the material, which have wavelength dependence, are specified in the material statement itself. A particular wavelength has an associated absorption coefficient. Varying the bias applied to the front and back contacts keeping the wavelength of the incident light constant generates the I-V characteristics. Keeping the bias constant and varying the wavelength of the incident light generate the Spectral Response. A sample program is shown below which will help the reader better understand the tool, its syntax and intricacies.

Appendix I (continued)

$ A program to simulate light I-V characteristics

TITLE HgI2

$ Definition of simulation mesh

MESH

X.MESH WIDTH=100 H1=5

$ Mesh definition along the X direction

Y.MESH DEPTH=600 H1=15 H2=15 h3=15

$ Mesh definition along Y direction

REGION NAME=HGI2 SEMICOND

ELECTRODE NAME=FRONT_CONTACT TOP

ELECTRODE NAME=BACK_CONTACT BOTTOM

$ Contact definition along with position

$ HgI2 is defined as belonging to the semicond group and the properties are defined

$ below

MATERIAL SEMICOND EG300=2.13 AFFINITY=4.00 PERMITTI=11

$ Band-gap, electron affinity and permittivity

MATERIAL SEMICOND NC300=2.0E+19 NV300=2.0E+19

$ Density of states

Appendix I (continued)

MATERIAL SEMICOND

+ WAVE.IM=(0.4,0.41,0.42,0.43,0.44,0.45,0.46)

+ ABSORPT=(6500,6400,6300,6200,6100,6000,5900)

$ Wavelengths and the corresponding absorption co-efficients

$ The + sign is used to continue the same statement on different lines

MATERIAL SEMICOND

+ WAVE.IM=(0.47,0.48,0.49,0.5,0.51,0.52)

+ ABSORPT=(5800,5700,5600,5500,5400,5300)

MATERIAL SEMICOND

+ WAVE.IM=(0.53,0.54,0.55,0.56,0.57,0.58,0.59,0.6,0.61,0.62,0.63,0.64)

+ ABSORPT=(5200,5100,2000,850,800,70,36,12,3,0.9,0.5,0.08)

MOBILITY SEMICOND MUN0=4 MUP0=0.5

$ Electron and hole mobilities

CONTACT NAME=FRONT_CONTACT

+ WORKFUNC=4.8 SURF.REC TRANSELE

+ VSURFP=1e+7 VSURFN=1e+7

$ A transparent non-ohmic contact is defined along with its work function and surface

$ recombination velocities

$ The TRANSELE parameter is used to set the contact as transparent

Appendix I (continued)

```
CONTACT            NAME=BACK_CONTACT
+             WORKFUNC=5.2 SURF.REC
+             VSURFP=1E+7 VSURFN=1E+7
TRAP          MIDGAP TAUN=1e-5 N.TOTAL=1e+10
TRAP          MIDGAP TAUP=1e-7 N.TOTAL=-1e+12
```

$ Electron and hole lifetimes

```
MOBIL              SEMICOND FLDMOB=2 REGION=HGI2
MODELS             FLDMOB FERMIDIR REGION=HGI2
```

$ Field mobility model and Fermi-Dirac statistics are used as simulation models

```
SYMB          CARRIER=2 NEWTON
PHOTOGEN  RAYTRACE X.ORG=50 Y.ORG=-5 WAVELENG=0.5825
+ FLUX=6E+15
```

$ Initialization of a light source with incident wavelength and incident flux

$ X.ORG and Y.ORG specify the location of the sample with respect to the light source

```
SOLVE INIT
```

$ Initialization of simulation

```
SOLVE V(FRONT_CONTACT)=0
SOLVE V(BACK_CONTACT)=0
```

$ Both contacts are first set to 0V

Appendix I (continued)

SOLVE V(FRONT_CONTACT)=0 VSTEP=0.5 NSTEP=120

$ The front contact bias is increased by +0.5V at each step upto 60V

$ The back contact is maintained at 0V

$ This section of the program generates the light I-V characteristics under + bias

PLOT.1D X.AXIS=V(FRONT_CONTACT) Y.AXIS=I(FRONT_CONTACT)

+ BOTTOM=0 TOP=1.5E-10 LEFT=-70 RIGHT=+70

$ The plot of photocurrent v/s applied bias is generated

SOLVE V(FRONT_CONTACT)=0

SOLVE V(FRONT_CONTACT)=0 +VSTEP=-0.5 NSTEP=120

$ The front contact bias is increased by -0.5V at each step upto -60V

$ The back contact is maintained at 0V

$ This section of the program generates the light I-V characteristics under - bias

PLOT.1D X.AXIS=V(FRONT_CONTACT) Y.AXIS=I(BACK_CONTACT) UNCH

$ The UNCH parameter plots both + and – bias currents on the same graph